JGR Oceans

RESEARCH ARTICLE
10.1029/2020JC016092

Special Section:
Contributions from the Physics of Estuaries and Coastal Seas meeting, 2018

Mechanisms of Exchange Flow in an Estuary With a Narrow, Deep Channel and Wide, Shallow Shoals

W. Rockwell Geyer[1], David K. Ralston[1], and Jia-Lin Chen[2]

[1]Department of Applied Ocean Physics and Engineering, Woods Hole Oceanographic Institution, Woods Hole, MA, USA, [2]Department of Hydraulic and Ocean Engineering, National Cheng Kung University, Tainan, Taiwan

Key Points:
- The exchange flow in Delaware Bay is confined to the channel region
- The mechanism of exchange flow is dominated by density-driven exchange flow during neap tides and by tidal dispersion during spring tides
- Lateral density gradients cause enhanced lateral exchange that contributes both to the residual circulation and oscillatory salt flux

Correspondence to:
W. R. Geyer,
rgeyer@whoi.edu

Citation:
Geyer, W. R., Ralston, D. K., & Chen, J.-L (2020). Mechanisms of exchange flow in an estuary with a narrow, deep channel and wide, shallow shoals. *Journal of Geophysical Research: Oceans*, *125*, e2020JC016092. https://doi.org/10.1029/2020JC016092

Received 3 FEB 2020
Accepted 20 OCT 2020
Accepted article online 29 OCT 2020

Abstract Delaware Bay is a large estuary with a deep, relatively narrow channel and wide, shallow banks, providing a clear example of a "channel-shoal" estuary. This numerical modeling study addresses the exchange flow in this channel-shoal estuary, specifically to examine how the lateral geometry affects the strength and mechanisms of exchange flow. We find that the exchange flow is exclusively confined to the channel region during spring tides, when stratification is weak, and it broadens laterally over the shoals during the more stratified neap tides but still occupies a small fraction of the total width of the estuary. Exchange flow is relatively weak during spring tides, resulting from oscillatory shear dispersion in the channel augmented by weak Eulerian exchange flow. During neap tides, stratification and shear increase markedly, resulting in a strong Eulerian residual shear flow driven mainly by the along-estuary density gradient, with a net exchange flow roughly 5 times that of the spring tide. During both spring and neap tides, lateral salinity gradients generated by differential advection at the edge of the channel drive a tidally oscillating cross-channel flow, which strongly influences the stratification, along-estuary salt balance, and momentum balance. The lateral flow also causes the phase variation in salinity that results in oscillatory shear dispersion and is an advective momentum source contributing to the residual circulation. Whereas the shoals make a negligible direct contribution to the exchange flow, they have an indirect influence due to the salinity gradients between the channel and the shoal.

Plain Language Summary Delaware Bay is a large estuary with a deep, relatively narrow channel and wide, shallow banks, providing a clear example of a "channel-shoal" estuary. This numerical modeling study addresses the exchange flow, that is, the two-way transport that provides continual exchange of water and waterborne material between the estuary and the ocean. This study examines how the particular lateral geometry of the channel-shoal estuary affects the strength and mechanisms of exchange flow. We find that the exchange flow is generally confined to the channel region, even more so during the times of maximum tidal forcing. The study also addresses the mechanisms of exchange flow—particularly the role of tidal processes compared to the flow resulting from the density contrast between fresh water entering the estuary from riverine sources and high-salinity oceanic water at the mouth. The study finds that tidal processes dominate during the peak tidal amplitude, that is, spring tides, and density-driven processes dominate during minimum tidal amplitude, that is, neap tides. During both spring and neap tides, the lateral variation in salinity is an important driving force for the residual circulation as well as the tide-induced salt transport.

1. Introduction

The classical paradigm for the estuarine circulation developed by Pritchard (1954) and Hansen and Rattray (1965) focused on the along-estuary and vertical structure of velocity and salinity, without considering the significance of the lateral dimension. Likewise, the more recent consideration of tidal nonlinearities on the estuarine circulation by Jay and Musiak (1996) and the influence of tidal straining on stratification by Simpson et al. (1990) considered only the along-estuary and vertical coordinates.

However, the importance of lateral variability has been recognized by many authors, including Nichols (1972), Wong (1994), Valle-Levinson et al. (2000), and Waterhouse and Valle-Levinson (2010). The interaction between lateral advection and along-estuary dispersion was examined in the groundbreaking but often overlooked theoretical papers by Smith (1977, 1982). The observations of axial convergence fronts by Nunes and Simpson (1985) provided field confirmation of Smith's theoretical work.

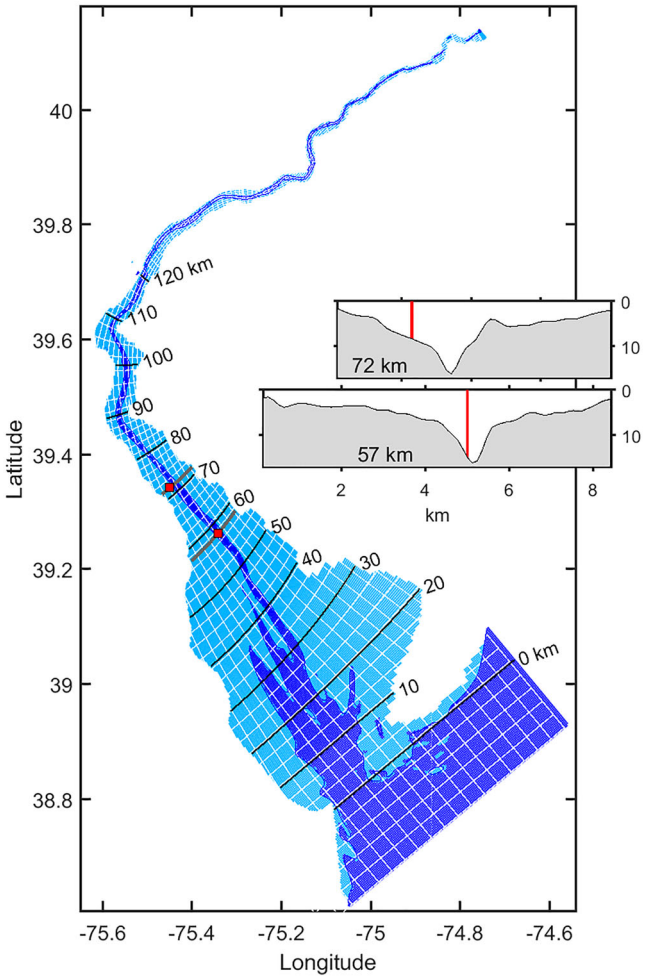

Figure 1. Map of Delaware Bay, with the numerical grid superimposed, showing every tenth grid line. Dark blue shading indicates depths >10 m, and light blue indicates depths <10 m. Two mooring locations are indicated, one on the flank and the other in the channel, and cross sections at those locations are shown in the insets.

Whereas the topic of tidal straining has mainly considered the along-estuary component (starting with Simpson et al., 1990), the observations of lateral straining by Lacy et al. (2003) demonstrated that stratification may be more dependent on lateral than along-estuary straining, causing maximum stratification to occur during the flood rather than the ebb tide. This result has been confirmed by several other studies, including Ralston and Stacey (2005), Scully and Geyer (2012), Becherer et al. (2015), and Schulz et al. (2015). The Schulz et al. study is particularly relevant to the present work, as it demonstrates the coupling between the lateral circulation induced by differential advection and the restratification of the estuary at the end of the flood tide. This contrasts the one-dimensional paradigm for tidal straining, which leads to maximum stratification at the end of the ebb. Schulz et al. demonstrate that this flood-tide restratification significantly augments the longitudinal straining during the subsequent ebb, contributing markedly to the eddy-viscosity shear correlation (ESCO) mechanism driving the residual circulation. However, the ESCO mechanism is not the only nonlinear mechanism contributing to the enhanced circulation. Lateral advection makes a direct contribution to the residual velocity structure, as demonstrated originally by Lerczak and Geyer (2004) in idealized numerical simulations and confirmed with the more realistic numerical study by Scully et al. (2009) and field observations by Becherer et al. (2015).

In considering the influence of lateral processes on salt transport, it is important to distinguish the contribution of the residual circulation from that of tidal dispersion. Hansen and Rattray (1965, 1966) defined the parameter ν, the fraction of the total salt flux caused by tidal dispersion, as a nondimensional means of assessing the relative roles of residual circulation and tidal dispersion in the salt flux. The analysis of salt transport in salinity coordinates, often called total exchange flow (TEF) (Chen et al., 2012; MacCready, 2011; Wang et al., 2017), combines the contribution of the Eulerian residual shear and the tidal oscillatory flux into the incoming and outgoing branches of the exchange flow. While the TEF approach provides a rigorous quantification of the exchange flow, the estimation of ν is more appropriately performed in an Eulerian framework. It would be valuable to determine how lateral processes affect the TEF as well as the partitioning between residual transport and tidal dispersion.

This paper builds on the recent advances in quantifying the role of lateral processes on longitudinal exchange, most notably the Schulz et al. and Becherer et al. studies of the role of lateral processes on longitudinal exchange. This study contrasts the Schulz et al. study in that it considers the realistic geometry of Delaware Bay, with much more abrupt lateral transitions in depth than their idealized study. Thus, it addresses the dynamics of the common class of estuaries with a narrow channel and broad flats. In addition to addressing the influence of lateral processes on the residual circulation, this study points out the particular significance of tidal dispersion in estuaries with distinct channel-shoal geometry, echoing and amplifying the results of Ralston and Stacey (2005). In addition, this paper uses the TEF framework to unify the influences of tidal and residual transport processes on the estuarine kinematics.

Delaware Bay (Figure 1) has a distinctive "channel-shoal" morphology, with a narrow, dredged channel approximately 1 km wide and lateral shoals that extend as much as 10 km on either side. This type of estuarine geometry is not uncommon; other examples include South San Francisco Bay, Mobile Bay, and even the mouth of the Chang Jiang estuary. Aristizábal and Chant (2014) demonstrated that the channel-shoal configuration leads to strong lateral salinity gradients, which drive lateral cells and cause lateral, tidal straining of the stratification that causes maximum stratification during the flood tide. This

is the same process that was first identified by Lacy et al. (2003) in San Francisco Bay and subsequently found by Ralston and Stacey (2005) in a shallow, intertidal regime, by Scully and Geyer (2012) in the Hudson estuary, by Schulz et al. (2015) in idealized simulations, and by Becherer et al. (2015) in the German Wadden Sea. As in these other cases, the lateral advection may influence the estuarine exchange flow both due to its influence on stratification and by its advective contribution to the momentum balance of the shear flow.

This paper addresses the mechanisms responsible for the salt balance in Delaware Bay, with particular attention to the influence of the channel-shoal geometry on the stratification, exchange flow, and salt flux. In the next section, the numerical model configuration is described, including comparison with observations to assess its fidelity with the actual Delaware Bay regime. The second section presents the TEF methodology for quantifying the exchange flow and the more conventional Eulerian decomposition. The results are presented in section 3, and the implications are discussed in section 4.

2. Methods

2.1. Numerical Simulations

The Regional Ocean Modeling System circulation model (Haidvogel et al., 2008) was used to simulate the hydrodynamics of Delaware Bay. The domain extends from the Atlantic Ocean to the head of tides at Trenton, NJ, approximately 190 km from the mouth (Figure 1). The curvilinear grid is $1{,}276 \times 184$ in the horizontal with 20 vertical sigma levels. The average grid spacing is roughly 100 m in the cross-estuary direction and 165 m in the along-estuary direction (note that every tenth grid line is shown in Figure 1). The model setup is essentially the same as that described by Chen et al. (2018), in which realistic simulations of Delaware Bay were used to explore the influence of surface wave dynamics. That paper provides a skill assessment of the model.

The focus of this paper is a set of simulations with realistic tidal forcing and constant river discharge over a range of magnitudes. The constant river discharge was selected to allow a clear quantification of the influence of spring-neap variability without the confounding influence of discharge variability. Tidal forcing includes semidiurnal, diurnal, fortnightly, and monthly variations of water level and currents. Tides are forced by specifying the surface elevation along the seaward open boundary. The riverine forcing includes four cases with constant river discharge of 100, 300, 600, and 1,000 m^3/s, corresponding to 30%, 100%, 200%, and 300% of the mean discharge. For each case, a 60-day spin-up was performed, followed by a 40-day simulation. The spin-up period is required to get past the transient adjustment of salinity to the prescribed discharge conditions.

The numerical model was calibrated with observed flow velocities and salinity during the field experiments during several months of varying discharge condition in 2011 (Aristizábal & Chant, 2014; Chen et al., 2018). A comparison of the data with the model over several spring-neap cycles is shown in Figure 2. Along-estuary velocity well matches the observations at the mooring at 57 km (second panel). Stratification is a particularly important variable for this study, so the model predictions of stratification in the channel (third panel) and shoal (bottom panel) were compared with the observations. While there are short-time scale deviations, the amplitude and variability of the stratification are well represented by the model at these two locations. Model skill (Murphy, 1988; see details in Chen et al., 2018) for the prediction of salinity was in the range of 0.69 to 0.80, and the regression coefficient r^2 between observed salinities and the model was 0.74 to 0.79.

2.2. Quantification of Salt Flux

The analysis of the estuarine salt flux is intended to identify the transport mechanisms and to facilitate comparison of the rates and mechanisms between different estuaries. The traditional, Eulerian decomposition (Lerczak et al., 2006; Uncles et al., 1985) distinguishes the contribution of steady shear dispersion (commonly associated with the estuarine circulation) from the oscillatory dispersion processes associated with the tides. The fundamental balance as represented by MacCready and Geyer (2010) is

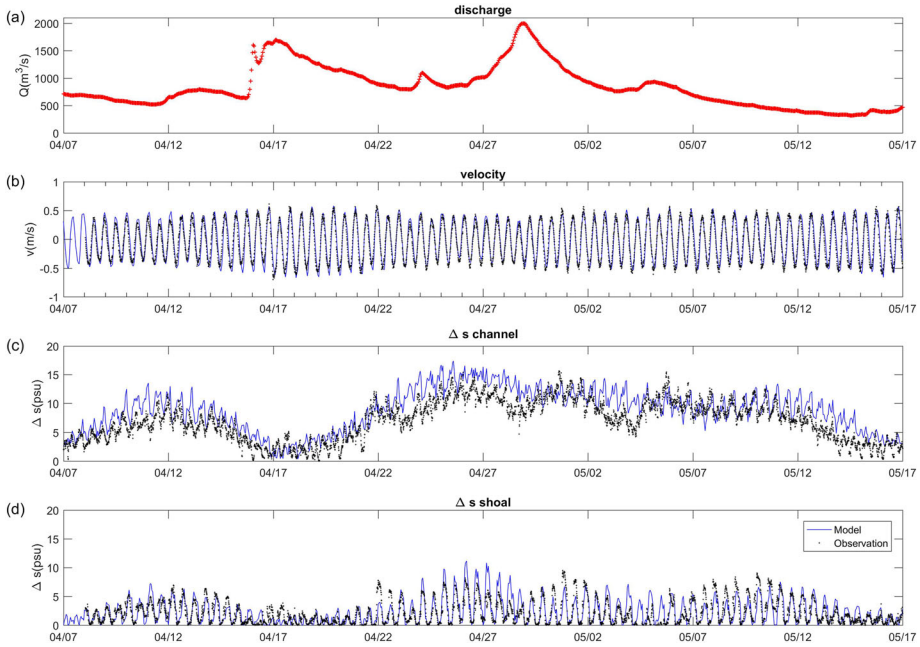

Figure 2. Calibration time series data for model, from a field study in the spring of 2011 reported by Aristizábal and Chant (2014). (a) is river discharge; (b) is the observed (black dots) and model-simulated (blue lines) depth-averaged velocity at the mooring at 57 km. (c) and (d) show observed (black dots) and modeled (blue lines) stratifications (as salinity difference between near-bottom and near-surface locations) for this time period at the channel mooring (57 km) and the shoal (72 km). The magnitude of the stratification, its spring-neap variability, and the difference between the shoal and the channel moorings are well resolved by the model.

$$\begin{aligned} Q_r\bar{s} &= \overline{Q's'} + \langle Q_T s_T \rangle - \frac{d}{dt}\int_{Volume} sdV \\ &\quad river \quad estuarine \quad tidal \quad storage \\ Q_r\langle \bar{s} \rangle &= \iint_{area} u's'dA + \iint_{area} \langle u_T s_T \rangle dA - \frac{d}{dt}\int_{Volume} sdV \\ &\quad river \quad estuarine \quad tidal \quad storage \end{aligned}, \tag{1}$$

where the overbar represents a cross-sectional average, Q_r is the time-averaged riverine outflow, u' and s' are time-averaged, cross-sectionally varying transport and salinity, u_T and s_T are tidal variations of velocity and salinity, and $\langle\rangle$ represents a tidal average. The first term is the seaward advection of salt due to the river outflow; the second is the "estuarine" circulation, although the driving forces for the residual circulation may include tidal nonlinearities in addition to the along-estuary baroclinic pressure gradient. The third term is the contribution of tidal correlations of velocity and salinity to along-estuary transport or tidal dispersion (Fischer et al., 1979). The importance of the tidal term is quantified by the parameter

$$\nu = \frac{\iint_{area} \langle u_T s_T \rangle dA}{Q_r \langle \bar{s} \rangle} \tag{2}$$

defined by Hansen and Rattray (1965, 1966) to represent the fraction of the total salt transport accomplished by tidal dispersion. The last term is the storage of salt, which is a measure of the unsteadiness of the salt balance (Banas et al., 2004; Lerczak et al., 2006). This is a useful definition for the steady regime, but a more robust definition of ν for the unsteady regime is

$$\nu = \frac{\iint_{area} \langle u_T s_T \rangle dA}{Q s_{tot}}, \tag{3}$$

where

$$Qs_{tot} = \iint_{area} u's'dA + \iint_{area} \langle u_T s_T \rangle dA, \tag{4}$$

that is, it includes the sum of the estuarine and tidal contributions to the flux.

An alternative approach is the TEF methodology (Chen et al., 2012; MacCready, 2011), which keeps track of the salt flux in salinity coordinates. The Eulerian approach allows the lateral and vertical structure of the exchange flow to be analyzed, as well as separating the tidal fluxes from the Eulerian residual exchange flow, while the TEF approach provides a concise measure of the magnitude of the exchange flow in terms of the quantities associated with the salt-balance equations of Knudsen (1900). In this paper we employ both the Eulerian and the TEF approaches, to provide the concise quantification afforded by TEF while using the Eulerian analysis to distinguish the influence of the lateral structure and tidal variability.

The application of the TEF approach follows MacCready (2011), in which the temporally and spatially varying transport at each cross section is binned into a number of salinity classes. In essence, the TEF method transforms the independent variable of the transport from spatial to salinity coordinates. For this analysis, the salinity bins represent a Δs of 0.5 psu, from 0 to 31 psu. The sensitivity of the result to the size of the salinity bin is discussed below. The binning process results in a three-dimensional array of transport (m^3/s) with dimensions of time, along-channel position, and salinity. In MacCready's notation, the transport is defined as $-\partial Q/\partial s$, so that the transport across a particular range of salinities is

$$Q(s_1 \rightarrow s_2) = \int_{s_1}^{s_2} -\partial Q/\partial s \, ds = \sum_{s_1}^{s_2} Q_i, \tag{5}$$

where Q_i is the volume transport in m^3/s within salinity bin s_i. In practice, the calculation of transport is a simple summation, so the awkward term $-\partial Q/\partial s$ does not need to be estimated directly. The next step in the TEF analysis is to filter out the tidal variation, for which a 43-hr Lancos low-pass filter is used in this case. (The rather long filtering time scale is required in an environment in which the residual motions are weak relative to tidal velocities.) Next, the exchange flow is calculated each time and along-estuary position by integrating the transport in salinity space. In a "normal" (as opposed to hypersaline) estuary, the integral starting from $s = 0$ will yield an outflow over some range of salinity classes and then reversing at some salinity bin to an inflow for the higher salinity bins. The outward transport Q_{out} is defined to be the extremum of the integral, the level of which is defined as the "reversal salinity" s_{rev} (Wang et al., 2017). This is the same as the "dividing salinity" defined by MacCready et al. (2018) and applied by Lorenz et al. (2019), in which it was noted that this approach provides a robust calculation of TEF even in well-mixed conditions. The inflow transport Q_{in} is integral from s_{rev} to the highest salinity bin.

$$\begin{aligned} Q_{out} &= \int_0^{s_{rev}} -\partial Q/\partial s \, ds = \sum_0^{s_{rev}} Q_i \\ Q_{in} &= \int_{s_{rev}}^{s_{max}} -\partial Q/\partial s \, ds = \sum_{s_{rev}}^{s_{max}} Q_i, \end{aligned} \tag{6}$$

Note that there may be multiple local extrema in the integral, particularly for weakly stratified estuaries, but s_{rev} is defined uniquely by the highest extremum of a given profile, which removes ambiguity from the calculation of Q_{in} and Q_{out} and minimizes the sensitivity of TEF to the choice of Δs. In these calculations, varying the size of Δs resulted in a few percent changes in the transport estimates.

The other TEF variables are s_{in} and s_{out}, which are readily calculated based on the salt fluxes in the outflowing and inflowing salinity classes:

$$\begin{aligned} s_{out} &= \frac{\int_0^{s_{rev}} s\,\partial Q/\partial s \, ds}{Q_{out}} = \frac{\sum_0^{s_{rev}} s_i Q_i}{Q_{out}} \\ s_{in} &= \frac{\int_{s_{rev}}^{s_{max}} s\,\partial Q/\partial s \, ds}{Q_{in}} = \frac{\sum_{s_{rev}}^{s_{max}} s_i Q_i}{Q_{in}}, \end{aligned} \tag{7}$$

The relationship between the TEF variables and the classical Eulerian salt balance can be determined by approximating the cross-sectionally averaged salinity by

$$\bar{s} \cong \frac{1}{2}(s_{in} + s_{out}). \tag{8}$$

While not exact, it is a good approximation in partially mixed estuaries, where these decompositions are the most relevant. Recasting 1 in terms of TEF variables,

$$\begin{array}{llll} Q_r\bar{s} & \cong & Q_{TEF}\Delta s & -\dfrac{d}{dt}\int_{Volume} sdV \\ river & & TEF\,salt\,flux & storage, \end{array} \tag{9}$$

or

$$\begin{array}{ll} Q_{TEF}\Delta s & \cong \quad Qs_{tot} \\ TEF\,salt\,flux & Eulerian\,salt\,flux, \end{array} \tag{10}$$

where $Q_{TEF} = 1/2(|Q_{in}| + |Q_{out}|)$ and $\Delta s = s_{in} - s_{out}$. For the remainder of the paper, the two terms in 10 will be referred to as Qs_{TEF} and Qs_E (where the subscript "E" here refers to "Eulerian"). Note that both the estuarine residual and tidal salt flux are included in the Eulerian salt flux, and together, these are equivalent to the TEF salt flux. For estuaries dominated by the Eulerian residual, Q_{TEF} approximately equals the Eulerian residual exchange flow. For tidally dominated regimes, that is, $\nu \approx 1$, Q_{TEF} is the tidally averaged volumetric exchange flow, which could not be determined from the Eulerian analysis. The advantage of TEF is that for any variation of the relative strengths of tidal and residual exchange, the volumetric exchange is consistently estimated, which allows the Knudsen analysis of volume and salt transport to be applied irrespective of the relative importance of tidal processes (see Chen et al., 2012; Sutherland et al., 2011; Wang et al., 2017, for illustrative examples in different estuarine regimes). The disadvantage of TEF is that the relative strength of the tidal and residual transports cannot be determined. That is why both methods are employed in this analysis.

3. Results and Analysis

3.1. Spring-Neap Variability

The most distinctive result of the Delaware Bay simulations is the spring-neap variability of the stratification, exchange flow, and salt flux. Strong spring-neap variability was evident for all four river discharge cases—here the 300 m^3/s case is selected to illustrate the sensitivity of the estuarine variables to the strength of the tidal forcing. Figure 3 shows the time variability of some key variables at a mid-estuary location (km 65) through the spring-neap cycle. The apogean neap tide occurs around Day 89, and strong spring tides occur around Days 80 and 96. Tidally averaged stratification in the channel (Δs thalweg) reaches a maximum during the neap, with a vertical salinity difference of 14 psu, and it weakens to 2–3 psu during spring tides. The salinity difference based on TEF (Δs) shows a similar value to the Eulerian subtidal stratification during spring tides, although it does not reach as high as the value during neaps. The TEF quantity represents the difference between flux-weighted inflow and outflow salinities, whereas the Eulerian Δs represents the maximum vertical difference, so the TEF quantity is smaller when the vertical variation of salinity is more important than temporal variability (e.g., neap tide conditions between Days 86 and 92). In the situations dominated by temporal variability, Δs TEF may be larger than Δs thalweg (e.g., spring tide conditions between Days 95 and 98).

The TEF exchange flow Q_{TEF} shows similar temporal variation as Δs, with a marked increase in the exchange flow during neap tides (Figure 3, third panel). The Eulerian residual shear (represented as vertical velocity difference Δv of the tidally averaged flow in the channel) shows a similar pattern as the TEF quantities, although the units are different. Estuarine salt flux was estimated based on the Eulerian quantities (Equation 1) as well as the TEF quantities (Equation 7). The estimates are almost exactly the same (Figure 3, fourth panel), indicating that the approximation for depth-averaged salinity in Equation 8 is quite accurate for the partially mixed regime. Both show a strong spring-neap variation, with more than a factor of 6 increase in the estuarine salt flux during neap tides.

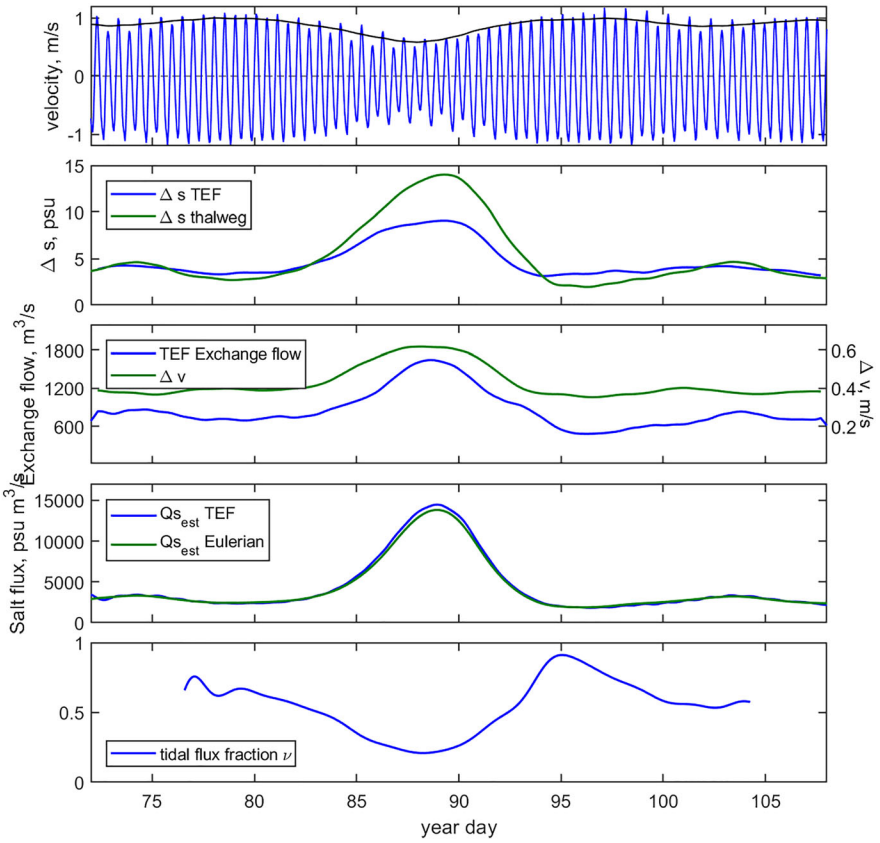

Figure 3. Temporal variation of key estuarine quantities for the 300 m^3/s simulation, at the along-channel location km 65. The top panel shows the tidal velocity in the center of the channel, showing the spring-neap variability over this interval with one pronounced neap tide around Day 89. The black line is the low-pass filtered tidal amplitude. The second panel provides a comparison of Δs from the total exchange-flow (TEF) calculation with the vertical salinity difference in the thalweg. The third panel includes Q_{TEF} (m^3/s) and the vertical velocity difference in the thalweg (m/s). The fourth panel compares the estuarine salt flux based on TEF (Equations 9 and 10) compared to the Eulerian estimate (Equation 4). The last panel shows the tidal fraction of salt flux ν (based on along-estuary averages of the fluxes between 50 and 85 km). The truncation of the plot of ν at the beginning and end of the record is due to the long time averaging required to produce a stable value of the tidal salt flux. The shaded bars indicate time intervals over which spring and neap conditions were averaged.

Finally, the ν parameter that indicates the fraction of salt flux due to tidal oscillatory shows considerable spring-neap variability (Figure 3, bottom panel). It reaches a value close to 1 during strong spring tides, indicating the dominance of tidal oscillatory processes, and gets as small as 0.2 during neaps, indicating the dominance of residual exchange flow during the neap. The ν parameter was found to exhibit strong variation over short along-estuary scales, as previously noted by Chen et al. (2012) and Wang et al. (2015) and explained by complex temporal/spatial interactions of the shear flow and topography. The values reported here represent along-estuary averages through the mid-estuary region (km 50–85), to minimize the influence of spatial variability, thus highlighting the spring-neap variation. Filter length considerably longer than a tidal cycle (71 hr) was required to distinguish oscillatory and residual fluxes, so the estimates of ν are truncated at the beginning and end of the record. The reason longer filter length is required for the calculation of ν was not determined definitively. A partial explanation is that the tidal variability of salt flux is much larger relative to its mean than either salinity or velocity. In addition, the inclusion of multiple tidal frequencies (M2, S2, N2, K1, and O1) causes a broader band of tidal energy than would one or two tidal components, requiring a longer filter length for a given reduction in tidal variance.

3.2. Stratification

The along-estuary salinity structure following the thalweg during springs and neaps (Figure 4) looks much like a typical, partially mixed estuary (e.g., the Hudson—cf. Geyer et al., 2000), with a relatively uniform

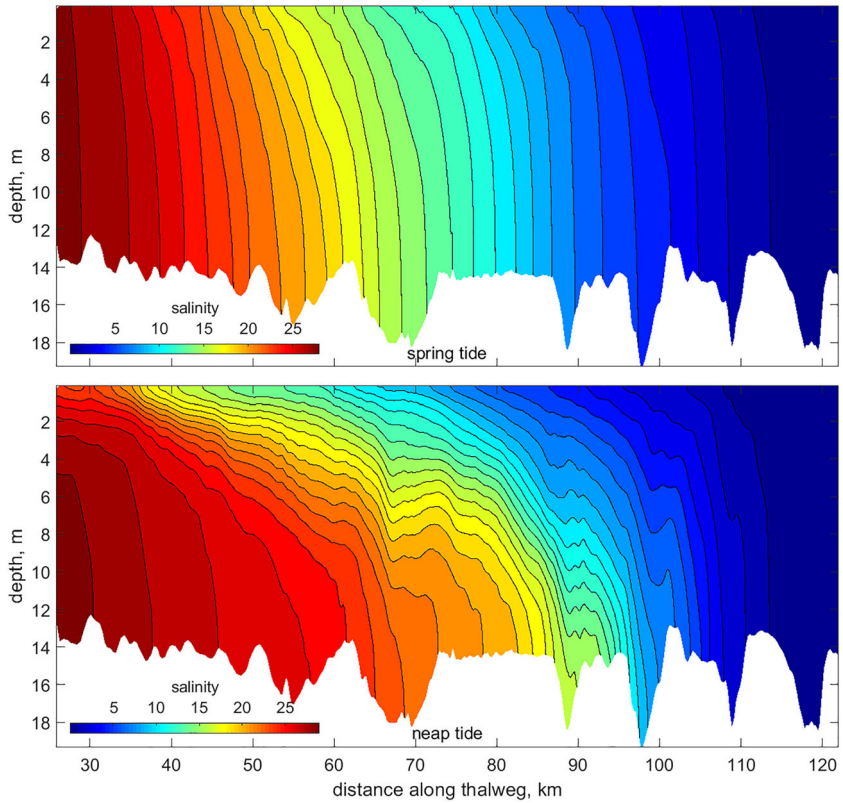

Figure 4. Along-channel sections within the thalweg of salinity for spring tide (Days 80 and 81—upper panel) and neap tide (Days 89 and 90—lower panel). In each case the model data have been averaged over 25 hr to remove tidal fluctuations. Slight stratification persists in the mid-estuary during spring tides, and stratification is strong throughout the thalweg during neaps.

longitudinal salinity gradient, nearly vertical isopycnals during spring tides, and tilted isopycnals during neap tides when stratification dominates. However, the lateral structure of stratification (Figure 5) indicates that the along-thalweg view is not characteristic of much of the estuary, in that the broad, shallow flats are unstratified during both spring and neap tides. During spring tides, stratification only occurs in the narrow band of the channel, roughly 1 km wide, compared with the overall estuary width of 10–20 km. During neap tides, the zone of stratification spreads laterally to be several km in width, but it is still confined to the channel and its adjacent flanks, with most of the shoal regions remaining unstratified.

The strength of the stratification of an estuary depends on the competition between straining and mixing, as quantified by the Simpson number (Geyer & MacCready, 2014; Simpson et al., 1990; Stacey & Ralston, 2005)

$$\mathrm{Si} = \frac{-\beta g(\partial s/\partial x)h^2}{\mathrm{C_d}{u_B}^2}, \tag{11}$$

where β is the proportionality between salinity and density anomaly, g is the acceleration of gravity, $\partial s/\partial x$ is the along-estuary salinity gradient, h is the local water depth, $\mathrm{C_d} \approx 3 \times 10^{-3}$ is the drag coefficient, and u_B is the amplitude of the near-bottom tidal velocity. Si can be used to diagnose tidal straining—the variation of stratification due to the tidal flow itself (Simpson et al., 1990)—or alternatively gravitational straining—the stratification resulting from the baroclinically induced shear (Li et al., 2018). Here we are considering both interpretations—the former to generate tidally periodic stratification and the latter to generate persistent stratification through the tidal cycle. The threshold value of Si for either mechanism has not been definitively established in the literature (Burchard & Schuttelaars, 2012; Stacey & Ralston, 2005), in part because different studies make different choices with respect to temporal and spatial averages of the variables. Li et al. (2018) used the same definitions as those described above in an

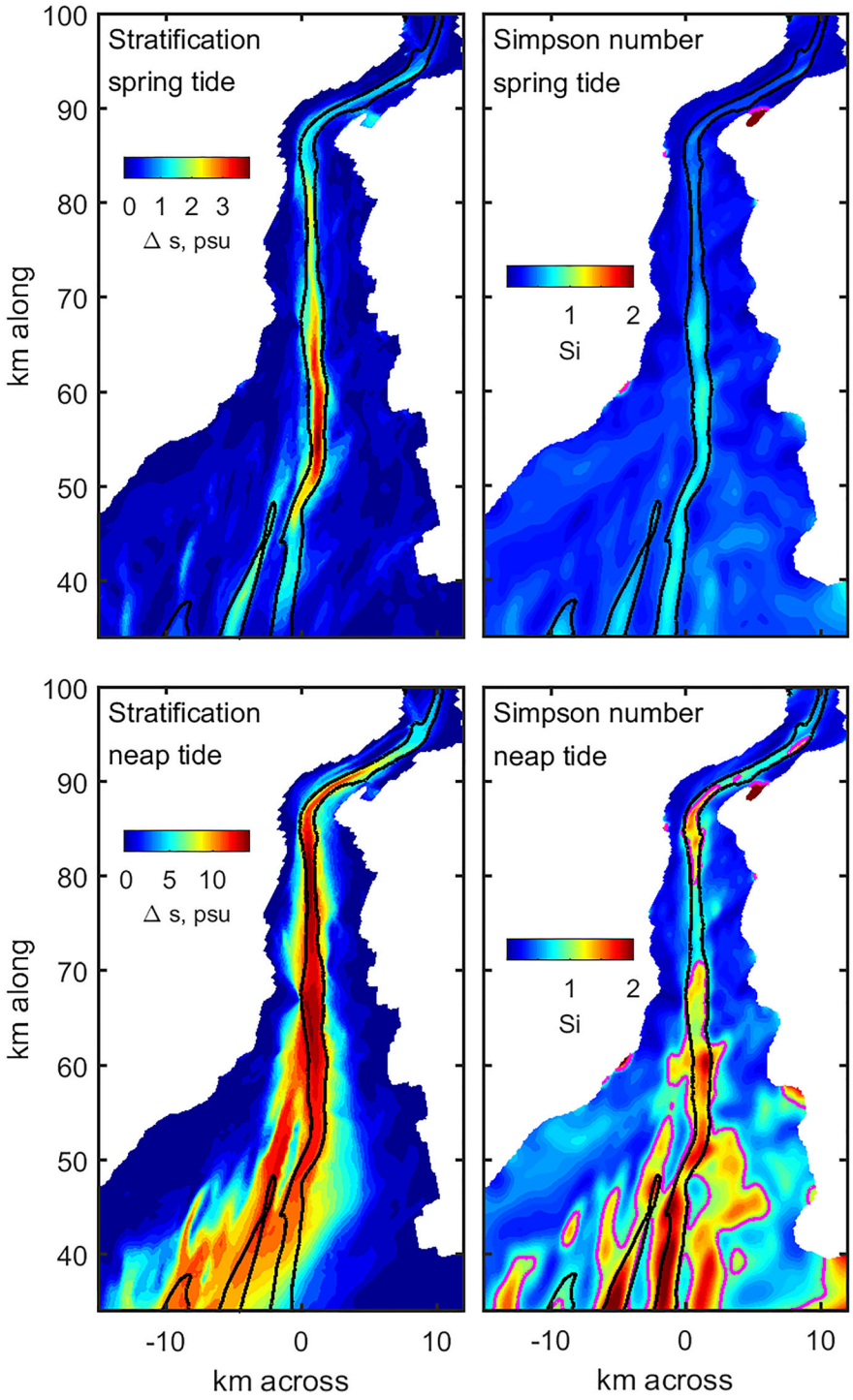

Figure 5. Plan view of stratification and Simpson number for spring (Days 80 and 81, upper panel) and neap (Days 89 and 90, lower panel), corresponding to the same time intervals as Figure 4. Stratification is reported as the difference between tidally averaged near-bottom and near-surface salinity. Simpson number is based on the along-channel salinity gradient, determined based on the direction of the principal axis of the tides. Values of Si = 1 are shown with a pink contour. The salinity gradient was averaged over 10 km in along-channel and cross-channel direction, whereas the velocity data were averaged over 3 grid points in *x* and *y*. The 10-m isobath is shown as a solid black line. The rectangles indicate the boundaries of the zoom-in shown in Figure 6.

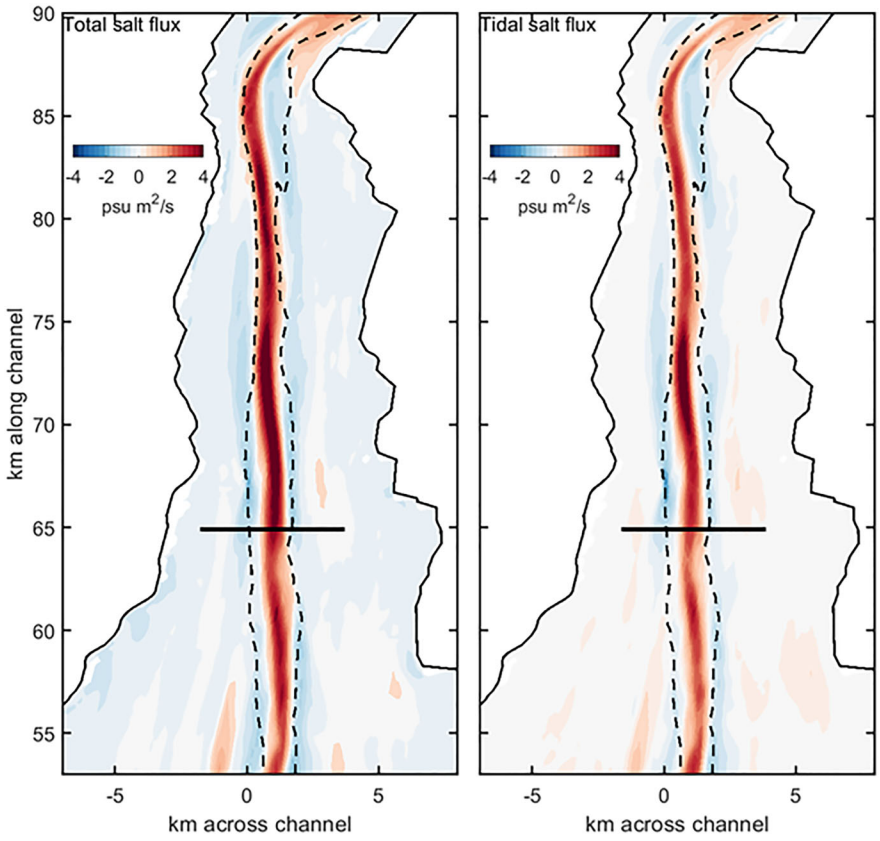

Figure 6. Vertically integrated salt flux (based on Eulerian calculations—Equation 4) for spring tides (Days 80 and 81) in the central portion of the estuary (corresponding to the rectangular box in Figure 5). Left panel = total salt flux; right panel = tidal component (due to tidally fluctuating velocity and salinity). Note that both quantities are strongly landward in the channel and close to zero on the flanks. The 10-m isobath is shown as a dashed black line. The solid line at 65 km shows the location of the sections shown in Figure 7.

analysis of a numerical simulation of the Chang Jiang estuary, finding that a threshold value of 1 appears to separate stratified and unstratified regimes.

Estimates of the Simpson number during spring and neap tides (Figure 5, lower panels) show that Si is persistently less than 1 on the shoals, even during neap tides, consistent with the absence of stratification there. In the channel, Si is typically slightly less than 1, with a few localized occurrences of Si ≈ 1, consistent with the weak and localized stratification in the channel during the spring tides. The neap tide distribution of Si shows considerable occurrence of Si > 1 in the channel and deeper troughs near the mouth, with values locally exceeding 2. The distribution of Si suggests that mixing processes are always strong enough to overcome the straining by the longitudinal salinity gradient on the shoals, and only during weak neap tides does straining become strong enough in the channel to overcome mixing. Note that the Simpson number as calculated based on the along-estuary salinity gradient does not account for lateral straining processes, which are particularly important along the flanks of the channel during the transition from flood to ebb, as previously described by Lacy et al. (2003), Scully and Geyer (2012), and Becherer et al. (2015). With respect to this paper, the important finding is that the lateral straining is related to the same lateral advection processes that affect the along-estuary salt flux, discussed in the next section.

3.3. Quantification of Salt Flux

The salt flux was estimated both by the Eulerian method (Equation 1) and the TEF methodology (Equation 9). While the TEF method is most appropriate for quantifying the cross-sectionally integrated exchange flow, only the Eulerian approach can be employed to reveal the lateral distribution of the salt flux.

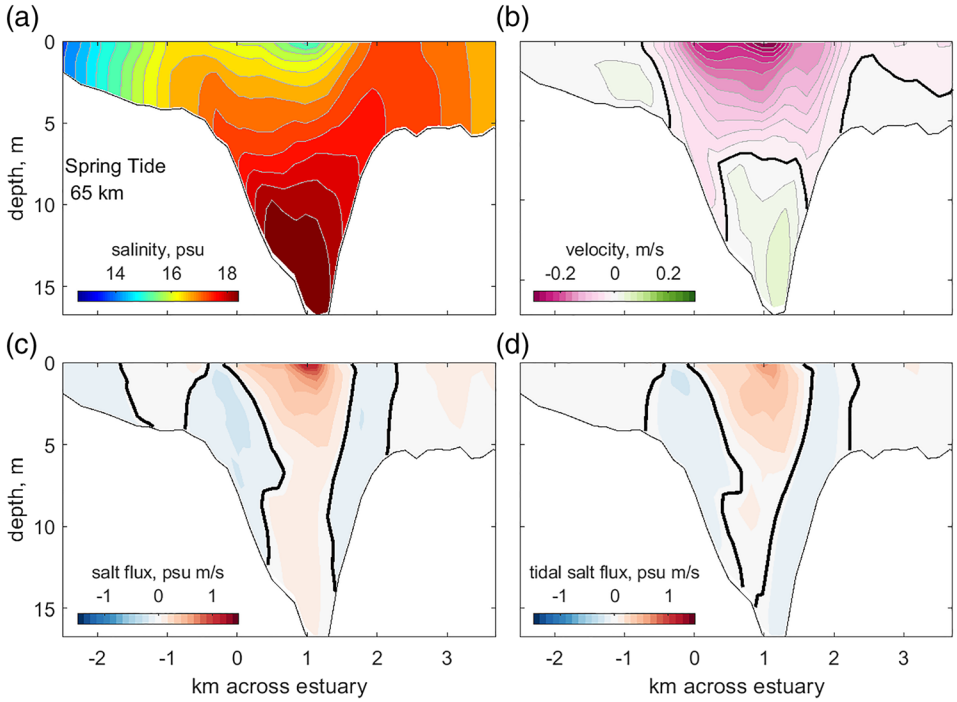

Figure 7. Spring-tide (Days 80 and 81) cross sections of salinity, velocity, and salt flux at km 65. (a) Tidally averaged salinity; (b) tidally averaged along-estuary velocity; (c) total salt flux; and (d) tidal salt flux. The solid lines in (b)–(d) show the zero contour. Stratification, shear, and salt flux are all prominent in the channel and weak on the flanks.

3.3.1. Spring Tides

A plan view of the depth-integrated, Eulerian salt flux distribution (Figure 6) during spring tides (300 m^3/s discharge) shows that the salt flux is largely confined to the channel. Within the middle portion of the estuary (between 50 and 85 km), 85% of the salt flux occurs in depths >7 m (contour line in Figure 6). The tidal oscillatory salt flux dominates in this middle segment, with $\nu = 0.62$ averaged over this 35-km section. The tidal salt flux also shows distinctive lateral variation, with a strong maximum in the center of the channel and weak reversal to seaward salt flux on the flanks.

A cross-sectional slice in mid-estuary (65 km; Figure 7) shows the lateral structure of the salt flux as well as tidally averaged salinity and along-estuary velocity. The salinity distribution indicates that tidally averaged stratification occurs only in the channel, with a vertical difference of around 2 psu. The residual velocity has a similar structure to salinity, with significant shear and surface outflow in the channel and very weak residual flow on the flanks. The salt flux is confined to the channel, as indicated previously, with a strong maximum near the surface associated with the salinity and velocity anomalies. The tidal oscillatory flux has a similar structure as the total salt flux, representing about two thirds of the total flux at this section during strong spring tides. The remainder of the flux is due to the product of the tidally averaged salinity and tidally averaged velocity, which shows strong correlation in the channel and essentially no contribution on the flanks, consistent with the absence of salt flux on the flanks. The oscillatory salt flux (as well as the total salt flux) shows weak reversals of salt flux at the flanks of the channel.

In order to understand the mechanism of tidal oscillatory salt flux, it is helpful to consider the tidal variation of velocity and salinity within the cross section. Salinity, along-channel velocity, and cross-channel velocity are shown in Figure 8 at the end of flood and the mid-ebb. The arrows show a lateral circulation structure with counterrotating cells at the end of the flood tide (top panels), which advect low-salinity water from the flanks into the upper part of the channel. This double circulation cell was first described by Nunes and Simpson (1985) in context with axial convergence fronts. Here we show how this lateral circulation affects the along-estuary tidal oscillatory salt flux.

As these circulation cells meet, a strong downward velocity develops in the middle of the channel (start ebb, middle panels), depressing the pycnocline and thereby increasing the area of the low-salinity water within

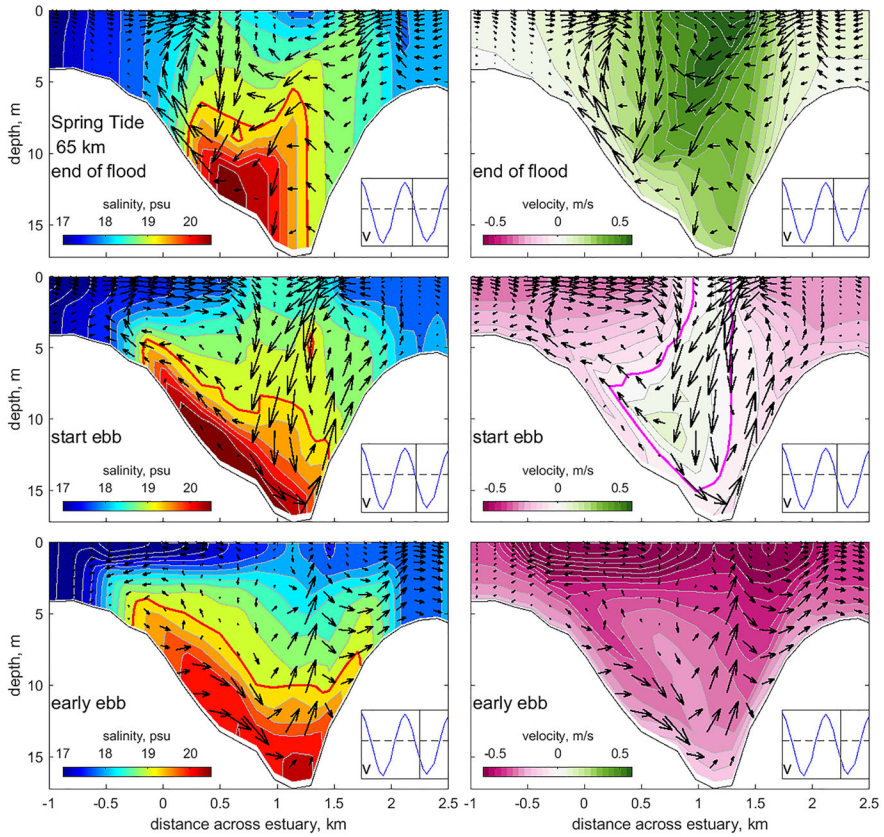

Figure 8. Spring-tide (Days 80 and 81) cross sections of conditions at 65 km close to high water. Left panels show salinity contours, with lateral and vertical velocity superimposed. Right panels show along-estuary velocity contours (green = up-estuary; pink = down-estuary), again with superimposed velocity arrows. Maximum horizontal velocity arrows are ~0.2 m/s, and maximum vertical velocities are ~0.001 m/s. These magnitudes are large enough to significantly alter the salinity structure over the two hours of near-slack-water conditions. Small insets show the tidal velocity over 24 hr to indicate the phase of the tide for each panel.

the channel. By the time strong ebb flow develops in the channel (lower right panel), the lateral circulation has produced a low-salinity anomaly over most of the region of strong outflow (lower left panel). The lateral circulation effectively lowers the salinity in the upper channel so that the negative salinity anomaly is partially in phase with the increasing ebb velocity, thereby producing a net salt flux.

This mechanism of shifting the phase of salinity with respect to velocity by baroclinically induced lateral advective motions was previously described by Smith (1982) in an analytic framework. This differs from the classic oscillatory shear dispersion mechanism (e.g., Fischer, 1972) in which lateral diffusion is responsible for the phase shift. In section 3.5, the phase shift will be discussed further, in order to come up with scaling for the magnitude of the tidal oscillatory salt flux.

3.3.2. Neap Tides

While the salt flux is much stronger during neap tides than spring tides, the plan view (Figure 9) indicates that the flux is still dominantly confined to the channel. During neap tides, the contribution of tidal oscillatory flux is a much smaller fraction of the total—the tidal dispersive fraction $\nu = 0.22$ averaged over the mid-estuary during neaps. As with the spring tide, ν shows considerable along-estuary variability, but on average, the residual shear and stratification are much more important to the salt flux than oscillatory flux.

Cross sections at 65 km during neaps show a very different structure from the spring tides (Figure 10), explaining the dominance of mean Eulerian salt flux. The channel is highly stratified, with more than 10-psu vertical salinity difference, and the along-channel velocity is highly sheared, with more than 0.5 m/s difference between the surface outflow and bottom inflow. This leads to a strong net salt flux,

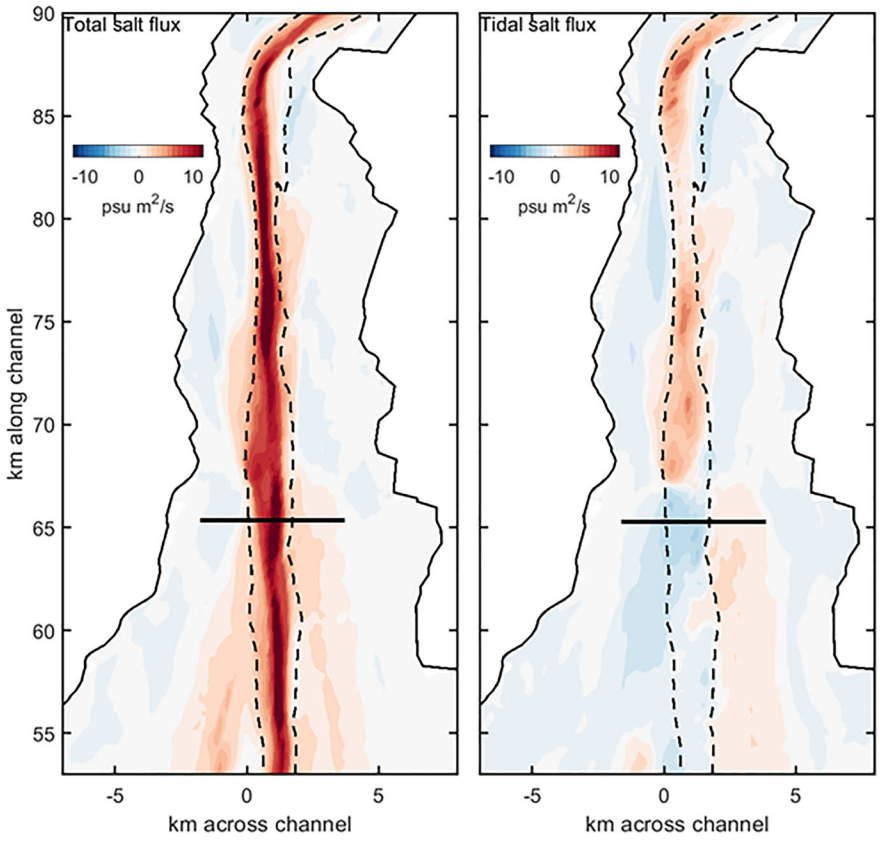

Figure 9. Vertically integrated salt flux for neap tides (Days 89 and 90). Left panel = total flux; right panel = tidal flux. As in spring tides, the flux is dominated by the channel, but note that the scale has been more than doubled relative to Figure 6, with much stronger fluxes during neap tides (cf. Figure 3, fourth panel).

with virtually all of the flux contributed by the strong surface outflow of low salinity water and bottom inflow of high salinity water in the channel (lower left panel). The negative flux in the middle of the water column in the channel is due to mean outflow of relatively high-salinity water, but it is much smaller in magnitude than the positive salt flux contributions. As shown in the plan view (Figure 9), the flanks make a minor contribution to the flux, even though stratification extends into the flanks, because the shear flow is confined to the channel. Tidal oscillatory flux at this location (lower right panel) is not significant, as noted above by the small value of ν.

3.4. Time Dependence of the Salt Balance

Averaged over multiple spring-neap cycles, salt is conserved in the Delaware model, as it must be in the real Delaware Bay. However, the large variation of salt flux between neaps and springs means that the salt content of the estuary is not constant at the spring-neap time scale, as evident by the spring-neap variation in the volume-averaged salinity ($\overline{s}$) as well as the variation in volume-averaged freshwater fraction (Figure 11, top panel). The freshwater fraction (Sheldon & Alber, 2006) is the fraction of fresh water that would need to be added to seawater in order to reach the estuary-average salinity, defined as

$$ff = \frac{s_o - \overline{s}}{s_o}, \tag{12}$$

where s_o is the maximum salinity entering the estuary. The volume-averaged salinity decreases during spring tides and abruptly increases during the weak neap. The freshwater fraction behaves exactly inversely from salinity (by definition), with fresh water accumulating during spring tides and rapidly being expelled during the neap. The transport of fresh and salt water is readily calculated by the TEF variables:

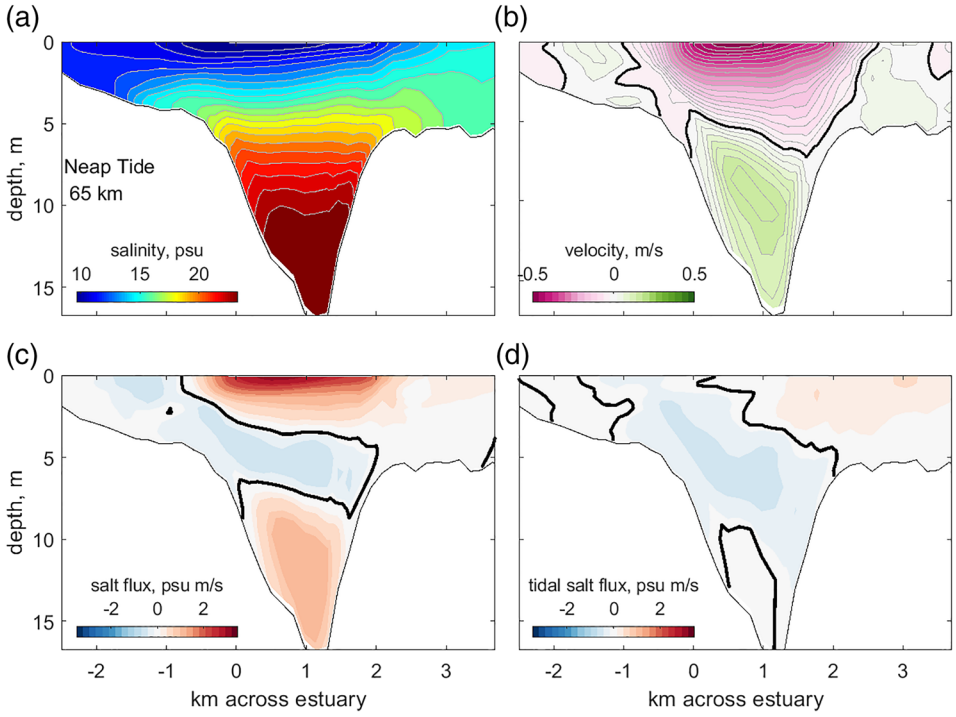

Figure 10. Neap-tide (Days 89 and 90) cross sections of salinity, velocity, and salt flux at km 65 (as with Figure 7 but with increased magnitude of all of the variables). The salt flux generally follows the structure of the residual velocity, except in the middle of the water column where a countergradient salt flux occurs as a result of tidal oscillatory processes.

$$\begin{aligned} Q_{in,\,fresh} &= Q_{in}(s_o - s_{in})/s_o \\ Q_{in,\,salt} &= Q_{in}s_{in}/s_o, \end{aligned} \tag{13}$$

and likewise for the corresponding Q_{out} variables. These quantities are shown in the middle panel of Figure 11. Both freshwater and saltwater transport increase markedly during neaps, with the biggest increases associated with the freshwater outflow and the saltwater inflow. While it is not surprising, it is important to note that there is always landward freshwater transport—this is recycled fresh water that is mixed into the lower layer on its way out of the estuary.

More relevant to the time variation of freshwater content and salinity is the cross-sectionally integrated freshwater and saltwater transport (Figure 11, bottom panel), obtained simply by summing the inflows and outflows. First, we note that the barotropic flow is the difference of the TEF inflow and outflow:

$$Q_{baro} = Q_{in} - Q_{out}. \tag{14}$$

Note that $Q_{baro} = -Q_r$ for steady-state conditions, but it varies due to barotropic fluctuations and is typically negative due to the contribution of the freshwater outflow. The net saltwater flux $Q_{net,salt}$ and net freshwater flux $Q_{net,fresh}$ can be approximated in terms of Q_e and Δs:

$$\begin{aligned} Q_{net,\,salt} &= Q_{TEF}\Delta s/s_o - Q_{baro}\bar{s}/s_o \\ Q_{net,\,fresh} &= -Q_{TEF}\Delta s/s_o + Q_{baro}(s_o - \bar{s})/s_o \\ &= -Q_{TEF}\Delta s/s_o + Q_{baro}ff. \end{aligned} \tag{15}$$

The last expression indicates that the estuarine salt transport plays a similar role in the freshwater balance as in the salt balance, except with the opposite sign. The stronger the estuarine salt flux, the stronger the freshwater outflow. The net salt transport is outward during spring tides and inward during neaps, consistent with the integrated salinity variations. If the estuary was always in steady state with respect to salt balance, the net salt transport would be zero. The net freshwater transport is always outward, but its

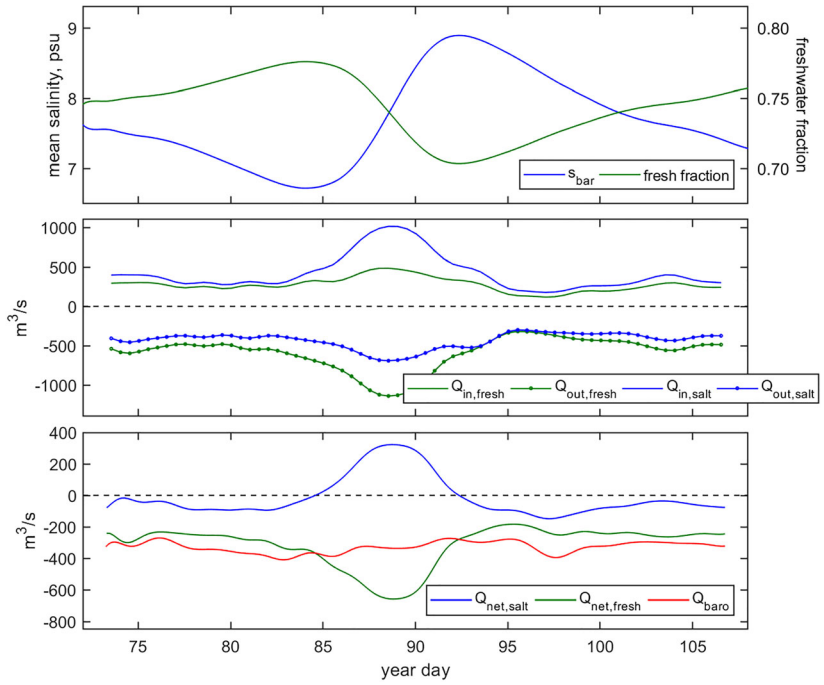

Figure 11. Time series of freshwater content and freshwater fluxes based on TEF analysis. Upper panel = average freshwater fraction and salinity based on volume integrals of the entire estuary landward of 65 km. A background salinity s_o = 30 psu was used for estimating the freshwater fraction. Middle panel = freshwater inflow and outflow and saltwater inflow and outflow. Lower panel = net seawater transport, net freshwater transport (Equations 12 and 13), and total barotropic transport (due to river outflow).

magnitude is less than the barotropic outflow during spring tides, and it significantly exceeds the barotropic outflow during neaps.

Note that the time dependence of the salt balance is directly related to the strength of the freshwater outflow relative to the barotropic flow, which on average is equal to the river discharge. During neap tides (e.g., Day 89) when the exchange flow is at its maximum, the freshwater outflow greatly exceeds the barotropic outflow, which means the estuary is rapidly losing fresh water. This is indicated by the steep decline in freshwater fraction during the neap (Figure 11, top panel). By mass conservation, if it is losing fresh water, it must be gaining salt water, which is indicated by the steep rise in s_{bar} (top panel) and the peak in $Q_{net,salt}$ (bottom panel). During nonneap conditions, when exchange flow is relatively weak, the freshwater transport is weaker (less negative) than the barotropic (Figure 11 bottom panel), and fresh water accumulates in the estuary (top panel: fresh fraction increasing). While this is an obvious consequence of conservation of freshwater volume, it is not generally recognized how the freshwater and saltwater balances are two sides of the same coin.

3.5. Dynamics of the Exchange Flow

While the above analysis indicates that the influence of the exchange flow on the salt and freshwater balances is the greatest during neap tides, a significant volumetric exchange flow persists through both springs and neaps (Figures 3, third panel; 7, and 10). Here we examine the driving mechanisms for the residual circulation finding that the baroclinic pressure gradient is the leading term, with significant contributions from lateral momentum advection as well as the ESCO mechanism.

3.5.1. Spring Tides

First, we note that during spring tides, there is a notable mean outflow in the channel (Figure 7b). However, the tidally averaged surface slope is negligible (estimated in the channel at the same location as Figure 7), and the vertically integrated pressure gradient in the channel (including the contribution of the along-estuary salinity gradient) is distinctly landward, with a magnitude of ~3×10^{-5} m s^{-2} (roughly one fifth of the maximum tidal pressure gradient). The contribution of the tidally averaged stress divergence

was estimated based on low-pass filtering of hourly estimates of the stress divergence $\partial/\partial z(K\partial v/\partial z)$, where K is the eddy viscosity. In the bottom water, the pressure gradient is balanced by net bottom stress, as would be expected in the classical estuarine balance (Geyer et al., 2000; Hansen & Rattray, 1965; Pritchard, 1956). However, at the surface, the stress divergence is still significant, with a magnitude of around 2×10^{-5} m s^{-2}, whereas the pressure gradient is close to zero. The surface stress divergence appears to be balanced by lateral advection, consistent with the findings of Lerczak and Geyer (2004) and Scully et al. (2009). This advective contribution is evident in the cross sections in Figure 8, which indicate that the lateral velocity carries low-momentum fluid into the channel at the end of the flood, reducing the net flood momentum and thereby generating a net seaward momentum contribution to the channel, which balances the mean stress divergence associated with the exchange flow. Although a precise calculation of the advective contribution to the momentum balance was not performed, the estimation of the tidally averaged contribution of $u\partial v/\partial y$ is of comparable magnitude to the stress divergence.

The relatively strong tidally averaged shear flow and weak pressure gradient forcing suggest that perhaps the eddy-shear covariance (ESCO) may explain the strength of the residual shear flow. This mechanism has been proposed as an alternative to the density-driven residual shear, and idealized simulations (e.g., Burchard & Hetland, 2010) have shown it to be of potential significance in weakly stratified regimes such as Delaware Bay. The ESCO shear arises from the time correlation of the vertical eddy viscosity K and the vertical shear du/dz, typically with weaker values of K during ebbs leading to stronger shears during ebbs and thus contributing to the residual shear (Jay & Musiak, 1996). The calculation of the ESCO shear velocity was performed following Burchard and Hetland (2010), where

$$u_{ESCO}(z) = -\int_{-H}^{z} \frac{\langle K' \partial u'/\partial \zeta \rangle}{\langle K \rangle} d\zeta + u_{bot}, \tag{16}$$

where again K is the eddy viscosity, the primes indicate time deviations from the tidal average, ζ is the vertical coordinate with respect to the integral, $\langle\rangle$ indicates tidal averaging, and u_{bot} is the near-bottom velocity (the last term is a simplification of the expression in Burchard and Hetland, 2010, but it does not alter the spatial structure of the result). The minus sign in 16 is consistent with the idea that the time-varying eddy coefficient provides a source term in the momentum equation that has to be balanced by an enhanced mean shear, that is, $\partial u_{ESCO}/\partial z$.

For the section at 65 km, we find a significant contribution of the ESCO mechanism in some parts of the cross section during spring tides, consistent with the stronger stratification and thus weaker eddy viscosity during the ebb. However, ESCO only explains a fraction of the mean shear, and its structure differs considerably from the observed mean shear (Figure 12, left panels). While ESCO makes a significant contribution to the mean shear, the dominant term driving the mean shear is the baroclinic pressure gradient, as in the classic Pritchard (1954) balance of the estuarine momentum equation. Lateral advection is also a significant contributor to the vertical shear in the upper water column. As noted earlier in this section, the lateral advection term is a dominant contributor to the tidally averaged momentum balance. Some of the fine-scale deviations between the ESCO velocity and the residual velocity in Figure 12 are qualitatively explained by the additional contribution of the lateral advection term. The regions on the flanks of the channel where the ESCO velocities are reversed are exactly the locations where lateral advection is maximal, as illustrated by the convergent near-surface velocities on the first two panels of Figure 8.

3.5.2. Neap Tides

While the residual velocity and salinity structure are very different during neap tides than during spring tides due to stronger stratification (Figure 10), the momentum balance is similar. The surface slope is small, and the bottom pressure gradient is due entirely to the contribution of the along-estuary salinity gradient, which balances the tidally averaged stress divergence in the lower layer. The tidally averaged stress divergence in the upper layer is close to zero, in spite of the strong mean shear. Again, tidally varying lateral advection appears to contribute to the out-estuary shear in the upper layer. In this case the stratification in the upper water column leads to low stress in the upper layer through the tidal cycle, with a tidal average stress divergence that is negligible. However, there is a slight landward-directed pressure gradient in the upper water column, with a magnitude of ~1×10^{-5} m s^{-2}. Just as during the spring tides, lateral advection provides a

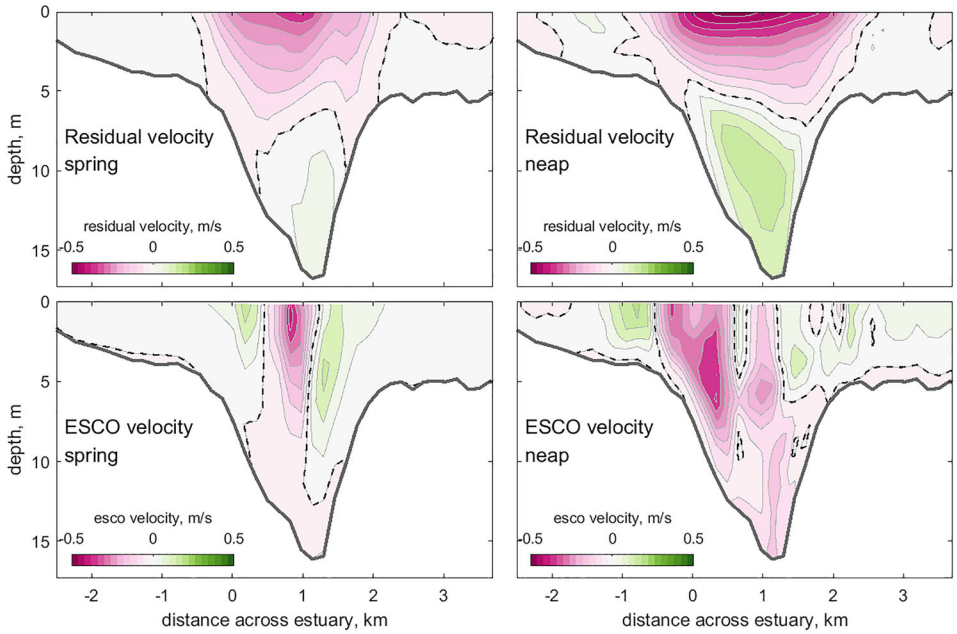

Figure 12. Residual velocity compared to ESCO velocity calculation for spring (Days 80 and 81) and neap tides (Days 89 and 90) at the section at 65 km. During spring tides, the maximum ESCO velocity is comparable to the residual velocity in the middle of the channel, but it has much less lateral extent and a substantially different lateral structure. The difference is even more pronounced during neap tides.

net seaward contribution to the momentum in the upper layer when averaged over the tidal cycle, with a magnitude roughly half of its value during spring tides. This relatively modest advective forcing is adequate to produce the strong out-estuary shear flow due to the strong stratification leading to minimal influence of stress divergence in the upper layer during neap tides.

Again, the ESCO calculation shows some enhancement of shear but with significant lateral deviations relative to the observed mean shear flow (Figure 12, right panels). Just as during spring tide conditions, the mean shear flow is driven by a combination of mean baroclinic and lateral advective forcing, with ESCO contributing to but not dominating the mean shear.

3.6. Sensitivity of Exchange Flow to River Discharge

While the main emphasis of this paper is on the spring-neap variability of the channel-shoal regime, model runs were also performed with different river discharge values to determine if the same findings applied across the range of discharge conditions typically experienced through the annual cycle. The first analysis is to consider the dependence of the spring-neap averaged exchange flow on discharge and then to examine how the spring-neap variability is manifested for different river discharge values.

The record-length averages (Table 1) show that the exchange flow increases with river discharge with a power law $Q_e \propto {Q_R}^{0.38}$. This is slightly greater than the value of 1/3 predicted by classical estuarine theory (MacCready & Geyer, 2010; Ralston & Geyer, 2019). The Eulerian residual velocity shear in the thalweg ($\Delta v_{thalweg}$) shows a significantly smaller exponent of 0.22, which is similar to the exponent of the salinity gradient ($\partial s/\partial y_{thalweg}$) of 0.20. These findings indicate that while the strength of the residual shear scales with the baroclinic pressure gradient (as predicted by linear theory), the magnitude of the exchange flow increases more strongly with discharge than the velocity shear. This may be explained in part by the exchange flow occupying a larger fraction of the cross section as the discharge increases, due to increased stratification allowing the exchange flow to extend slightly onto the flanks of the channel. Another factor that may cause Q_e to increase is increased spatial correlation (both vertical and lateral) between velocity and salinity at higher stratification conditions.

The variation of stratification with discharge is best represented by $\Delta s_{thalweg}$, which has dependence of river discharge of ${Q_r}^{0.60}$. When normalized by the local salinity $\bar{s}_{thalweg}$, the exponent increases to 0.72, which is

Table 1
Estuarine Exchange Flow Variables for Different River Discharges

Variables	100 m^3/s	300 m^3/s	600 m^3/s	1,000 m^3/s	Exponent	r^2
$Q_{e\ TEF}$ (m^3/s)	889	1,216	1,545	1,887	0.35	0.99+
$\Delta v_{thalweg}$ (m/s)	0.30	0.37	0.43	0.48	0.22	0.99+
Δs_{TEF} (psu)	3.4	4.8	6.2	7.7	0.38	0.99+
$\Delta s_{thalweg}$ (psu)	2.9	5.1	6.5	8.7	0.58	0.99+
$\bar{s}_{thalweg}$ (psu)	23.2	21.4	19.3	17.9	−0.12	0.98
$\Delta s_{thalweg}/\bar{s}_{thalweg}$	0.13	0.24	0.39	0.56	0.70	0.99+
$-\partial s/\partial y_{thalweg}$ (psu/km)	0.26	0.32	0.36	0.39	0.17	0.99

Note. All of the variables are based on averages between 50 and 80 km for the entire record. The exponents listed are for the best fit power law dependence of each variable on discharge, that is, Q_r^n. The regression coefficients r^2 are shown for those fits.

slightly higher than the theoretical dependence of stratification on discharge of two thirds (MacCready & Geyer, 2010). Interestingly, the quantity Δs_{TEF} behaves very differently from $\Delta s_{thalweg}$ with respect to river discharge, with an exponent of 0.36 compared to 0.6 for $\Delta s_{thalweg}$. This difference is explained by the fact that Δs_{TEF} is not just a function of vertical salinity variation, but it also depends on tidal variations in salinity. For weakly stratified, low-discharge conditions, Δs_{TEF} is significantly augmented by the tidal variability, whereas during more strongly stratified, high-discharge conditions, the vertical salinity difference dominates, and the maximum vertical salinity difference $\Delta s_{thalweg}$ exceeds the transport-weighted Δs_{TEF}.

Now we consider the spring-neap variability of the salt flux for different discharge conditions (Figure 13 and Table 2). The general findings are consistent for all discharge conditions—the strong increase in salt flux from spring to neap tide, the large increase in stratification from spring to neap tide, and the dominance of salt flux in the channel ($Qs_{e\ channel}/Qs_{e\ total}$). While the salt flux increases as a function of discharge for both spring and neap conditions, it increases more steeply with discharge for the neap conditions. This means that as discharge increases, a larger fraction of the total salt flux occurs during the weak neap tides. This can be understood more clearly by noting the complementary nature of the salt flux and the freshwater flux, as described in context with Figure 11. This result thus indicates that most of the freshwater flux occurs during neap tides. This is true of all of the discharge conditions, but there is a lot more freshwater flux for the high-discharge regime, so as a consequence, the estuarine salt flux also shows a greater disparity between neaps and springs.

A comparison of the Eulerian estimate of salt flux with the TEF estimate indicates that they agree to within 10% or less for the most part, with the greatest discrepancies occurring at the highest discharge (Figure 13). These discrepancies arise from the discrepancy between the cross-sectionally averaged salinity $\bar{s}$ and the average of the TEF quantities s_{in} and s_{out} (Equation 8). When the exchange flow is significantly greater than the river flow (i.e., partially mixed conditions), this approximation is valid, but it becomes less so for high-discharge conditions. The generally good agreement between the two estimates provides support for the use of TEF for the quantification of estuarine exchange processes.

Interestingly, the tidal salt flux fraction ν is relatively insensitive to the variation in discharge, retaining its strong sensitivity to the spring-neap cycle for all discharge conditions. This indicates that the estuarine regime shifts between the tidal oscillatory mode during spring tides and the residual shear mode of salt flux during neap tides over this wide range of discharge conditions. At high discharge, the tidal oscillatory salt transport may also be influenced by tidal variations in the vertical structure of the stratification and shear, as described by Geyer and Nepf (1996). This type of salt transport should be regarded as tidal distortion of the residual shear-induced salt transport, rather than a tidal dispersive transport. It was not determined how much of the tidal salt transport may be accounted for by this mechanism, but it may explain the unexpected increase in ν at the highest discharge conditions.

3.7. An Effective Dispersion Coefficient

Following Lerczak et al. (2006), it is useful to express the magnitude of the estuarine salt flux in terms of an effective dispersion coefficient, that is,

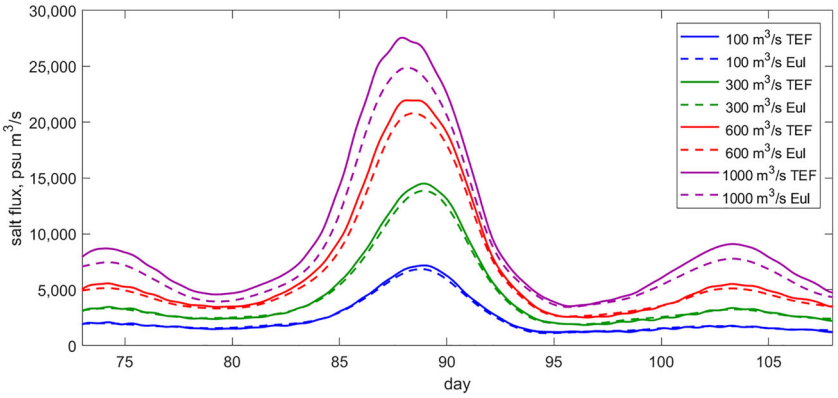

Figure 13. Time series of the estuarine salt flux based on the TEF and Eulerian estimates—Qs_{TEF} and Qs_E (Equation 10), for varying discharge. For all discharges, the estuarine salt flux is much greater during the neaps than spring tides, due both to increased stratification and increased exchange flow. For low-discharge conditions, the TEF and Eulerian estimates are nearly the same, but they differ for higher-discharge conditions due to inaccuracy of the approximation that the cross-sectionally averaged salinity is equal to the average of the TEF quantities S_{in} and S_{out} (Equation 8).

$$-AK\frac{\partial s}{\partial y} = Qs_{tot}, \tag{17}$$

where A is the cross-sectional area of the estuary. With units of m^2/s, K can be compared among estuaries and against different parameterizations for dispersion. However, based on the results of this study, it may not be appropriate to use the entire cross-sectional area of the estuary if the salt flux is dominated by a limited portion of the total area. For the case of Delaware Bay, a more informative estimate of K may come from considering only the salt flux in the channel and only the area of the channel. The portion of the salt flux on the shoals that is excluded is small, on the order of 20%, but the total area is 2–3 times the channel area. An estimate of the effective dispersion coefficient K_{eff} is based on the fraction of salt flux in the channel and the area of the channel, with values shown in Table 2. The large difference in the values between spring and neap reflects the large change in magnitude of salt flux and the relatively small change in $\partial s/\partial y$. The spring-tide values of K vary between 150 and 270 m^2/s, and the neap-tide values range from 640 to 2,100 m^2/s. These values are not dissimilar to estimates obtained by Lerczak et al. (2006) in the Hudson, with typical spring-tide values of 130 m^2/s and neap tide values up to a maximum of 2,600 m^2/s. As noted in the Lerczak study, the large change from neap to spring tides is related to a change

Table 2
Spring-Neap Variations of Salt Flux for Different River Discharges

	100 m^3/s		300 m^3/s		600 m^3/s		1,000 m^3/s	
	Spring	Neap	Spring	Neap	Spring	Neap	Spring	Neap
$Q_{e\ TEF}$ (m^3/s)	520	1,130	660	1,480	850	1,740	1,060	1,900
$Qs_{e\ Eulerian}$ (psu m^3/s)	1,600	**6,800**	2,500	**13,700**	3,300	**20,300**	4,000	**23,800**
Qs_{TEF} (psu m^3/s)	1,500	**7,100**	2,400	**14,300**	3,500	**21,500**	4,700	**26,100**
$\Delta s_{\ TEF}$ (psu)	2.9	6.3	3.6	9.8	4.1	12.4	4.3	13.7
$Qs_{e\ channel}/Qs_{e\ total}$	0.76	0.84	0.83	0.81	0.88	0.81	0.90	0.83
ν	**0.74**	0.26	**0.64**	0.22	**0.64**	0.22	**0.66**	0.26
$-\partial s/\partial y$ (psu/km)	0.28	0.24	0.34	0.29	0.37	0.29	0.37	0.28
K_{eff} (m^2/s)	150	**640**	180	**1,100**	210	**1,600**	270	**2,100**
K_{tidal} (m^2/s)	110	(170)	120	(240)	130	(350)	180	(550)
α	0.04	(0.1)	0.04	(0.2)	0.05	(0.3)	0.07	(0.4)
A_o	(3.7)	2.3	(3.5)	2.2	(3.0)	1.8	(2.3)	1.6

Note. The estimates are all based on averages between 50 and 80 km. The spring-tide values are based on tidal averages for Day 80 and the neap-tide values for Day 89. The channel is defined as the portion of the cross section with depths greater than 9 m. See section 3.7 for an explanation of the estimation of K_{eff} and α. See section 3.8 for an explanation of A_o. The parentheses indicate the cases where the scaling is not relevant, based on the value of ν. The bold-faced entries indicate notable magnitudes of those quantities—specifically the dominance of neap-tide salt transport and the large values of ν during spring tides.

from tidal dispersion to residual shear dispersion. The inverse relationship between tidal dispersion and tidal amplitude is not a characteristic of all estuaries—Banas et al. (2004) demonstrate the opposite spring-neap dependence of the longitudinal dispersion coefficient in Willapa Bay, a lagoonal estuary dominated by tidal dispersive processes throughout the spring-neap cycle, with stronger dispersion during springs. The important finding here is that Delaware Bay behaves like a partially mixed estuary with respect to its spring-neap variation of longitudinal dispersion, due to the brief period of restratification during neaps that dominates its net longitudinal dispersion.

In order to examine the specific contribution of tidal dispersion, the tidal dispersion K_{tidal} was estimated by scaling K_{eff} with the "diffusive fraction" ν:

$$K_{tidal} = \nu K_{eff}. \tag{18}$$

With the results shown in Table 2, the value of K_{tidal} is similar during spring tides for the 100, 300, and 600 m^3/s cases, with values between 110 and 130 m^2/s. These values can be compared to the conventional scaling for tidal dispersion based on analysis of Okubo (1973), Zimmerman (1986), and Chen et al. (2012)

$$K_{tidal} = \alpha \frac{{u_T}^2}{\omega}, \tag{19}$$

where u_T is the amplitude of the tidal velocity in the channel, ω is the radian frequency of the tide, and α is a nondimensional coefficient with a value that may reach 0.05 for efficient oscillatory shear dispersion or tidal trapping (Chen et al., 2012; Okubo, 1973; Zimmerman, 1986). With $\omega = 1.4 \times 10^{-4}$ s^{-1} and the average tidal velocity amplitude $u_T = 0.61$ m/s for spring tides and 0.44 m/s during neaps (averaged over the channel cross section), we obtain values of α for the range of discharge cases of 0.04 to 0.07 for spring tides and 0.1 to 0.4 during neap tides. The spring tide values for the lower-discharge cases are very close to the optimal value of 0.05 observed in previous studies, including in another channel-shoal estuary that is shorter and shallower than the Delaware and has an average ν of 0.6 (Conroy et al., 2020). We suggest that the lateral exchange of salt that occurs at tidal time scales between the shoals and the channel provides near-optimal conditions for oscillatory shear dispersion, explaining the values of α close to 0.05.

The much higher values of α during neap tides require another explanation, because oscillatory shear dispersion cannot produce such large values of α. One important consideration is that while the tidal dispersion is high, the residual shear dispersion is roughly four times larger for the neap tide cases, as evidenced by the values of ν ranging from 0.22 to 0.26. The strong stratification conditions of the neap tides provide conditions in which the vertical excursions of the halocline may result in a significant component of tidal dispersion, as described by Wang et al. (2015) in the Hudson River. It is likely that the high tidal dispersion during neap tides is not an independent dispersion mechanism but rather is a consequence of the tidal distortion of the residual shear dispersion.

3.8. Scaling the Strength of the Exchange Flow

The classical scaling of the estuarine circulation results in a proportionality between the baroclinic driving force due to the along-estuary salinity gradient and the frictional drag of the residual flow, expressed by Scully et al. (2009) as

$$u_E = \frac{1}{A_o} \beta g \frac{\partial s}{\partial x} \frac{h^2}{C_D u_B}, \tag{20}$$

where u_e is the estuarine exchange velocity, A_o is a nondimensional constant, and the other variables are defined the same as the Simpson number 11 except that in this case they represent averages across the channel. If the conventional scaling applies, then a similar value of A_o should be found for different forcing conditions (and perhaps for different estuaries). This scaling was applied to the Delaware, estimating the strength of the estuarine velocity by

$$u_E = \frac{Q_E}{A_{channel}/2}, \tag{21}$$

where $A_{channel}$ is the area of the channel. The channel was specified as the portion of the channel with a depth

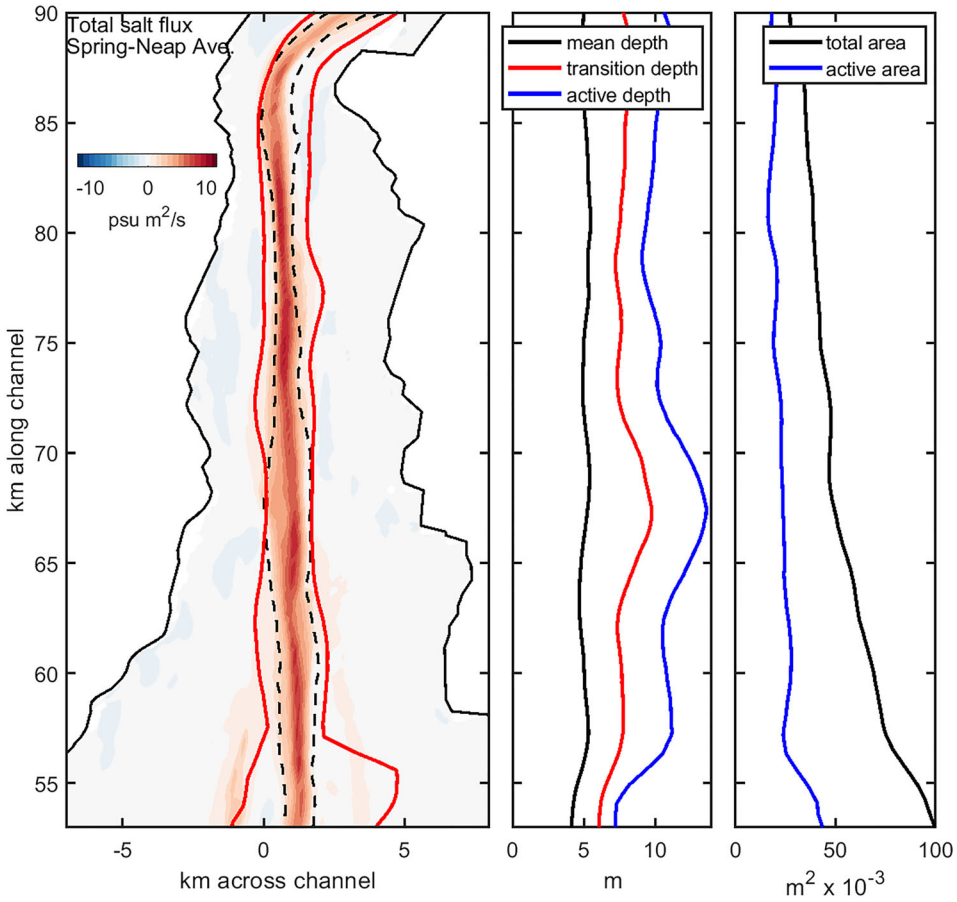

Figure 14. Along-estuary distribution of the "transition depth" defined by Equation 22as one half the thalweg depth. The left panel shows a comparison of the transition depth (red lines) to the spring-neap averaged salt flux distribution, showing that the significant salt flux is generally bounded by the transition depth. The dashed black line is the 10-m isobath. The middle panel shows an along-estuary comparison of the cross-sectional mean depth (black line), the transition depth (red) and the "active" depth, defined as the average of the depth exceeding the transition depth. The third panel shows the "active" area (i.e., bounded by the transition depth), compared to the total cross-sectional area.

greater than one half the maximum thalweg depth or 8–9 m. The estimate of $A_{channel}$ was not very sensitive to that choice, because of the abrupt transition at the edge of the dredged channel. (This issue is discussed further in the next section.) The expression 21 is based on the assumption that all of the exchange flow occurs in the channel and the inflow and outflow each occupy one half the cross-sectional area $A_{channel}$, which provides a reasonable approximation of the strength of the exchange flow for scaling purposes. When 21 is inserted into 20, we obtain an estimate of A_o, with the results shown in the last row of Table 2. The values for neap tides range from 2.3 for the lowest discharge case to 1.6 for the highest discharge. These numbers compare favorably with values obtained by Scully et al. (2009) for the Hudson River estuary, with values ranging from 2.3 to 1.9. The spring-tide values (in parentheses) are not relevant to this scaling, because most of the exchange flow is accomplished by tidal processes rather than the gravity-driven residual. The close agreement between the neap-tide scaling of the exchange flow in the Delaware and the Hudson scaling suggests that the dynamics responsible for the exchange flow are similar, and the strength of the exchange flow scales in proportion to the strength of the along-estuary salinity gradient. Note that the quantitative agreement between the Delaware and Hudson estimates of A_o depends critically on the selection of the channel area, rather than the total area, for the determination of the magnitude of u_E. If the total cross-sectional area were used, the magnitude of u_E would be reduced by a factor of 3, and the value of A_o would deviate by a factor of 3 from the Hudson values.

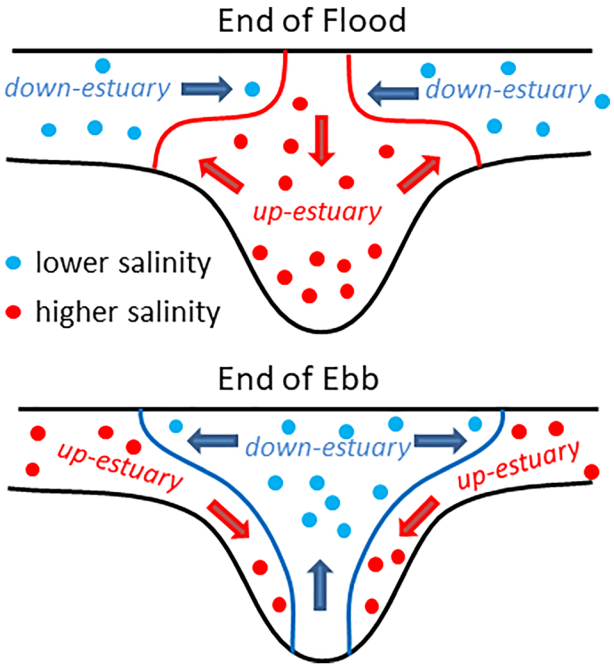

Figure 15. Cartoon schematic that demonstrates the influence of the lateral circulation on stratification and shear in the channel at the end of flood (upper panel) and end of ebb (lower panel). The upper panel corresponds to the model results shown in Figure 8. Differential advection during flood has produced higher salinities in the channel than the shoals, causing lateral gradients that drive a "lock exchange" on either side of the channel. This restratifies the channel and carries ebb-directed momentum into the surface layer. At the end of ebb, differential advection produces a reversed lateral gradient, which produces a reversed lock exchange, carrying dense water from the flanks into the deep water of the channel. This lateral exchange mechanism impacts the salt flux in three ways: It augments stratification of the channel; it augments the residual estuarine shear in the channel; and it advances the phase of salinity relative to velocity to augment tidal oscillatory flux.

4. Discussion

We now return to the question that motivated this paper—what is the influence of the channel-shoal geometry on the estuarine exchange flow? In terms of the magnitude and variability of the exchange flow, Delaware Bay is remarkably similar to the Hudson River, an estuary with no significant lateral shoals for much of its length. However, one of the keys to making the comparison between the Delaware and the Hudson is to consider that the "active" portion of the Delaware is the channel and its flanks and not to consider the broad, shallow regions in calculating the effective area of the estuary and related dynamical quantities. Attempts to "classify" estuaries should distinguish the "active" estuarine cross section in estimating quantities such as the net freshwater velocity and the average tidal velocity (cf., Geyer & MacCready, 2014). But how can the "active" cross section be determined a priori?

One simple approach based on the strong dependence of the salt flux on depth is to pick some fraction of the local thalweg depth as the transition from "active" to "inactive" cross section. The thalweg depth was determined based on the 95th percentile depth at each cross section, and a factor of 0.5 was chosen because it represents a factor of 4 decrease in the Simpson number from the thalweg to the shoal (considering only the depth dependence of Si and holding the other variables fixed).

$$h_{transition}(y) \approx 0.5 h_{thalweg}(y). \tag{22}$$

The position of the transition depth relative to the distribution of salt flux (for the average of spring and neaps) is shown in the left panel of Figure 14, and this transition depth roughly bounds the region of significant salt flux. While this approach does not completely capture the spatial variability of the flux, it provides a reasonable estimate of the effective width and area of the "active" cross section for the purpose of more effectively scaling the estuarine parameters. When the transition depth is used to bound the "active" cross section, the "active" depth is found to be more than twice as large as the laterally averaged (mean) depth. This is important for scaling the estuarine circulation which is particularly sensitive to depth (MacCready & Geyer, 2010). Similarly, the "active" area decreases to less than half of the total cross-sectional areas when limited by the transition depth. This is important for scaling the effective strength of freshwater forcing.

Another important scaling consideration is in context with the result of Schulz et al. (2015), who found that wide estuaries show little influence of lateral straining relative to intermediate width estuaries. Delaware Bay would definitely be in the "wide estuary" category based on the Schulz et al. analysis, yet its dynamics are strongly influenced by lateral straining. The resolution of this apparent paradox is that the transverse scale associated with the channel-shoal transition in Delaware Bay is not large—in fact that scale, on the order of 2 km, would put Delaware Bay into the category of an intermediate-width estuary, for which the lateral straining processes are dominant. This analysis suggests that it is not the total width of the estuary but rather the lateral scale associated with the transition from channel to shoals that determines the relative importance of lateral straining processes.

As to the influence of the channel-shoal geometry on the dynamics, this study indicates that the gradient in along-estuary velocity and salinity between the channel and the shoal have important consequences for the exchange flow. Differential advection of the along-estuary salinity gradient results in strong lateral salinity gradients, which provide a baroclinic driving force for lateral circulation, particularly at the slack water at the end of flood and ebb tides, when the lateral gradients are the largest (cf. Figure 8 for the flood-tide case). The lateral circulation provides both a mechanism for restratification of the channel and for the exchange of

momentum between the channel and the shoal, as shown schematically in Figure 15. In essence, lock exchange occurs in the lateral direction, with reverse orientation between flood and ebb. The lock exchange effectively converts the lateral salinity gradient to a vertical salinity gradient, thereby restratifying the channel (cf. Lacy et al., 2003, and associated references). While the actual process is more complicated due to along-estuary variability and the influence of planetary rotation, Figure 15 illustrates the baroclinic contribution to the lateral circulation.

In addition to influencing stratification, the lateral flow contributes to the net along-estuary shear flow in the channel. At the end of flood, velocities on the shoals reverse to the ebb direction earlier than the channel due to enhanced friction in the shallow water, so the near-surface transverse flow carries the ebb-directed momentum into the channel. The saltier, flood-directed current is directed out of the channel by the near-bottom lateral flow. The reverse happens at the end of ebb, due to the reversal of the channel-shoal salinity gradient. The net effect of the lateral momentum exchange during both slack tides is to augment the estuarine circulation in the channel—ebb directed in the upper layer and flood directed in the lower layer. This lateral advection is the advective momentum source that drives the mean out-estuary flow in the upper layer.

Not only does the lateral circulation contribute to the mean exchange flow, it also contributes to the tidal oscillatory salt flux and potentially explains the large effective dispersion coefficient discussed in section 3.7. In order for oscillatory salt flux to occur, the phase of the salinity variation has to be partially in phase with the velocity variation. The lateral flow accomplishes this by lowering the salinity in the channel at the end of the flood tide and raising it at the end of the ebb tide, thereby advancing the phase of the salinity variation, thus bringing it out of quadrature with velocity. The high values of ν during spring tides for all river discharge conditions (Table 2) indicate the importance of the oscillatory flux.

5. Summary and Conclusions

This modeling study indicates that the exchange flow in Delaware Bay is dominated by processes occurring in the channel and on its flanks, with the wide, shallow shoals making minor contribution to the exchange. The strength of the exchange flow varies markedly from spring tides to neaps, being approximately six times stronger during the weakest neap tides. During spring tides, oscillatory salt flux dominates over the Eulerian residual salt transport, whereas during neaps, most of the salt flux is due to the Eulerian mean shear in the presence of strong salinity stratification. Lateral flows induced by lateral salinity gradients between the channel and shoals are essential ingredients for maintaining stratification and net shear flow in the channel as well as for producing oscillatory salt flux. Although the shoals do not contribute directly to the salt flux, the tidally varying salinity gradient and shear between the shoals and the channel provide the driving mechanism for the oscillatory salt flux.

The coupling between differential advection and lateral salinity gradients as a mechanism for the generation of lateral flows is consistent with Lerczak and Geyer's (2004) idealized analysis, and the effect on the exchange flow is consistent with the analysis of two-dimensional strain-induced periodic stratification (SIPS) by Schulz et al. (2015). The oscillatory salt flux resulting from the tidal variation in lateral salinity gradient is consistent with the results of Ralston and Stacey (2005).

The dynamics and general estuarine characteristics of Delaware Bay are very similar to those of the Hudson River, in spite of a marked difference in estuarine geometry. This finding suggests that in order to properly diagnose the estuarine regime of an estuary with a deep channel and wide, shallow flanks, the "active" portion of the cross section has to be identified, and the dynamically relevant geometric variables such as depth and cross-sectional area need to be defined not based on the overall cross section but just within the "active" cross section. Using the "active" cross section, the scaling of the estuarine circulation as well as the strength of tidal dispersion is consistent with studies of other estuaries. This study demonstrates that multiple aspects of the estuarine geometry need to be considered in defining the key dynamical variables that lead to quantitative estuarine classification.

Data Availability Statement

Model data and analysis methods are available online (https://doi.org/10.26025/1912/25299).

Acknowledgments

The ideas in this paper were influenced by discussions with Robert Chant. Funding was provided by National Science Foundation grants OCE-1325136, OCE-1634490, and OCE-1736539.

References

Aristizábal, M., & Chant, R. (2014). Mechanisms driving stratification in Delaware Bay estuary. *Ocean Dynamics*, *64*(11), 1615–1629.

Banas, N. S., Hickey, B. M., MacCready, P., & Newton, J. A. (2004). Dynamics of Willapa Bay, Washington: A highly unsteady, partially mixed estuary. *Journal of Physical Oceanography*, *34*(11), 2413–2427.

Becherer, J., Stacey, M. T., Umlauf, L., & Burchard, H. (2015). Lateral circulation generates flood tide stratification and estuarine exchange flow in a curved tidal inlet. *Journal of Physical Oceanography*, *45*(3), 638–656.

Burchard, H., & Hetland, R. D. (2010). Quantifying the contributions of tidal straining and gravitational circulation to residual circulation in periodically stratified tidal estuaries. *Journal of Physical Oceanography*, *40*(6), 1243–1262.

Burchard, H., & Schuttelaars, H. M. (2012). Analysis of tidal straining as driver for estuarine circulation in well-mixed estuaries. *Journal of Physical Oceanography*, *42*(2), 261–271.

Chen, J.-L., Ralston, D. K., Geyer, W. R., Sommerfield, C. K., & Chant, R. J. (2018). Wave generation, dissipation, and disequilibrium in an embayment with complex bathymetry. *Journal of Geophysical Research: Oceans*, *123*, 7856–7876. https://doi.org/10.1029/2018JC014381

Chen, S. N., Geyer, W. R., Ralston, D. K., & Lerczak, J. A. (2012). Estuarine exchange flow quantified with isohaline coordinates: Contrasting long and short estuaries. *Journal of Physical Oceanography*, *42*(5), 748–763.

Conroy, T., Sutherland, D. A., & Ralston, D. K. (2020). Estuarine exchange flow variability in a seasonal, segmented estuary. *Journal of Physical Oceanography*, *50*(3), 595–613. https://doi.org/10.1175/JPO-D-19-0108.1

Fischer, H. (1972). Mass transport mechanisms in partially stratified estuaries. *Journal of Fluid Mechanics*, *53*(4), 671–687.

Fischer, H. B., List, J. E., Koh, C. R., Imberger, J., & Brooks, N. H. (1979). *Mixing in inland and coastal waters*. New York: Academic Press.

Geyer, W. R., & MacCready, P. (2014). The estuarine circulation. *Annual Review of Fluid Mechanics*, *46*, 175–197.

Geyer, W. R., & Nepf, H. (1996). Tidal pumping of salt in a moderately stratified estuary. In *Buoyancy effects on coastal and estuarine dynamics—Coastal and estuarine studies* (Vol. 53, pp. 213–226).

Geyer, W. R., Trowbridge, J. H., & Bowen, M. M. (2000). The dynamics of a partially mixed estuary. *Journal of Physical Oceanography*, *30*(8), 2035–2048.

Haidvogel, D. B., Arango, H., Budgell, W. P., Cornuelle, B. D., Curchitser, E., Di Lorenzo, E., et al. (2008). Ocean forecasting in terrain-following coordinates: Formulation and skill assessment of the Regional Ocean Modeling System. *Journal of Computational Physics*, *227*(7), 3595–3624.

Hansen, D. V., & Rattray, M. Jr. (1965). Gravitational circulation in straits and estuaries. *Journal of Marine Research*, *23*, 104–122.

Hansen, D. V., & Rattray, M. (1966). New dimensions in estuary classification1. *Limnology and Oceanography*, *11*(3), 319–326.

Jay, D. A., & Musiak, J. D. (1996). Internal tidal asymmetry in channel flows: Origins and consequences. *Coastal and Estuarine Studies*, 211–249.

Knudsen, M. (1900). Ein hydrographischer Lehrsatz. *Annalen der Hydrographie und Maritimen Meteorologie*, *28*, 316–320.

Lacy, J. R., Stacey, M. T., Burau, J. R., & Monismith, S. G. (2003). Interaction of lateral baroclinic forcing and turbulence in an estuary. *Journal of Geophysical Research*, *108*(C3), 3089. https://doi.org/10.1029/2002JC001392

Lerczak, J. A., & Geyer, W. R. (2004). Modeling the lateral circulation in straight, stratified estuaries. *Journal of Physical Oceanography*, *34*(6), 1410–1428.

Lerczak, J. A., Geyer, W. R., & Chant, R. J. (2006). Mechanisms driving the time-dependent salt flux in a partially stratified estuary. *Journal of Physical Oceanography*, *36*(12), 2296–2311.

Li, X., Geyer, W. R., Zhu, J., & Wu, H. (2018). The transformation of salinity variance: A new approach to quantifying the influence of straining and mixing on estuarine stratification. *Journal of Physical Oceanography*, *48*(3), 607–623.

Lorenz, M., Klingbeil, K., MacCready, P., & Burchard, H. (2019). Numerical issues of the total exchange flow (TEF) analysis framework for quantifying estuarine circulation. *Ocean Science*, *15*(3), 601–614. https://doi.org/10.5194/os-15-601-2019

MacCready, P. (2011). Calculating estuarine exchange flow using isohaline coordinates. *Journal of Physical Oceanography*, *41*(6), 1116–1124.

MacCready, P., & Geyer, W. R. (2010). Advances in estuarine physics. *Annual Review of Marine Science*, *2*, 35–58. https://doi.org/10.1146/annurev-marine-120308-081015

MacCready, P., Geyer, W. R., & Burchard, H. (2018). Estuarine exchange flow is related to mixing through the salinity variance budget. *Journal of Physical Oceanography*, *48*(6), 1375–1384. https://doi.org/10.1175/jpo-d-17-0266.1

Murphy, A. H. (1988). Skill scores based on the mean square error and their relationships to the correlation coefficient. *Monthly Weather Review*, *116*(12), 2417–2424. https://doi.org/10.1175/1520-0493(1988)116<2417:ssbotm>2.0.co;2

Nichols, M. M. (1972). Sediments of the James River estuary, Virginia. *Geological Society of America Memoirs*, *133*, 169–210.

Nunes, R. A., & Simpson, J. H. (1985). Axial convergence in a well-mixed estuary. *Estuarine, Coastal and Shelf Science*, *20*(5), 637–649.

Okubo, A. (1973). Effect of shoreline irregularities on streamwise dispersion in estuaries and other embayments. *Netherlands Journal of Sea Research*, *6*, 213–224.

Pritchard, D. W. (1954). A study of the salt balance in a coastal plain estuary. *Journal of Marine Research*, *13*(1), 133–144.

Pritchard, D. W. (1956). The dynamic structure of a coastal plain estuary. *Journal of Marine Research*, *15*, 33–42.

Ralston, D. K., & Geyer, W. R. (2019). Response to channel deepening of the salinity intrusion, estuarine circulation, and stratification in an urbanized estuary. *Journal of Geophysical Research: Oceans*, *124*, 4784–4802. https://doi.org/10.1029/2019JC015006

Ralston, D. K., & Stacey, M. T. (2005). Longitudinal dispersion and lateral circulation in the intertidal zone. *Journal of Geophysical Research*, *110*, C07015. https://doi.org/10.1029/2005JC002888

Schulz, E., Schuttelaars, H. M., Gräwe, U., & Burchard, H. (2015). Impact of the depth-to-width ratio of periodically stratified tidal channels on the estuarine circulation. *Journal of Physical Oceanography*, *45*(8), 2048–2069. https://doi.org/10.1175/jpo-d-14-0084.1

Scully, M. E., & Geyer, W. R. (2012). The role of advection, straining, and mixing on the tidal variability of estuarine stratification. *Journal of Physical Oceanography*, *42*(5), 855–868.

Scully, M. E., Geyer, W. R., & Lerczak, J. A. (2009). The influence of lateral advection on the residual estuarine circulation: A numerical modeling study of the Hudson River estuary. *Journal of Physical Oceanography*, *39*(1), 107–124.

Sheldon, J. E., & Alber, M. (2006). The calculation of estuarine turnover times using freshwater fraction and tidal prism models: A critical evaluation. *Estuaries and Coasts*, *29*(1), 133–146.

Simpson, J. H., Brown, J., Matthews, J., & Allen, G. (1990). Tidal straining, density currents, and stirring in the control of estuarine stratification. *Estuaries*, *13*(2), 125–132.

Smith, R. (1977). Long-term dispersion of contaminants in small estuaries. *Journal of Fluid Mechanics*, *82*(1), 129–146.

Smith, R. (1982). Contaminant dispersion in oscillatory flows. *Journal of Fluid Mechanics*, *114*, 379–398.

Stacey, M. T., & Ralston, D. K. (2005). The scaling and structure of the estuarine bottom boundary layer. *Journal of Physical Oceanography*, *35*(1), 55–71.

Sutherland, D. A., MacCready, P., Banas, N. S., & Smedstad, L. F. (2011). A model study of the Salish Sea estuarine circulation. *Journal of Physical Oceanography*, *41*(6), 1125–1143. https://doi.org/10.1175/2011jpo4540.1

Uncles, R. J., Elliott, R. C. A., & Weston, S. A. (1985). Observed fluxes of water, salt and suspended sediment in a partly mixed estuary. *Estuarine, Coastal and Shelf Science*, *20*(2), 147–167.

Valle-Levinson, A., Li, C., Wong, K. C., & Lwiza, K. M. (2000). Convergence of lateral flow along a coastal plain estuary. *Journal of Geophysical Research*, *105*(C7), 17,045–17,061.

Wang, T., Geyer, W. R., Engel, P., Jiang, W., & Feng, S. (2015). Mechanisms of tidal oscillatory salt transport in a partially stratified estuary. *Journal of Physical Oceanography*, *45*(11), 2773–2789.

Wang, T., Geyer, W. R., & MacCready, P. (2017). Total exchange flow, entrainment, and diffusive salt flux in estuaries. *Journal of Physical Oceanography*, *47*(5), 1205–1220.

Waterhouse, A. F., & Valle-Levinson, A. (2010). Transverse structure of subtidal flow in a weakly stratified subtropical tidal inlet. *Continental Shelf Research*, *30*(3–4), 281–292.

Wong, K. C. (1994). On the nature of transverse variability in a coastal plain estuary. *Journal of Geophysical Research*, *99*(C7), 14,209–14,222.

Zimmerman, T. F. (1986). The tidal whirlpool: A review of horizontal dispersion by tidal and residual currents. *Netherlands Journal of Sea Research*, *20*, 133–154.